The coronavirus helicase synergizes with the viral polymerase to enable rapid RNA synthesis through duplex RNA

Pim P. B. America[1,*], Subhas C. Bera[2,*], Arnab Das[1], Thomas K. Anderson[3], John C. Marecki[4], Flávia S. Papini[2], Jamie J. Arnold[5], Robert N. Kirchdoerfer[3], Craig E. Cameron[5], Kevin D. Raney[4], Martin Depken[6,#], David Dulin[1,2,#]

1. Department of Physics and Astronomy, and LaserLaB Amsterdam, Vrije Universiteit Amsterdam, De Boelelaan 1081, 1081 HV, Amsterdam, the Netherlands
2. Junior Research Group 2, Interdisciplinary Center for Clinical Research, Friedrich-Alexander-University Erlangen-Nürnberg (FAU), Cauerstr. 3, 91058 Erlangen, Germany
3. Department of Biochemistry and Institute for Molecular Virology, University of Wisconsin-Madison, Madison, WI 53706, USA
4. Department of Biochemistry and Molecular Biology, University of Arkansas for Medical Sciences, Little Rock, AR 72205, USA
5. Department of Microbiology and Immunology, University of North Carolina School of Medicine, Chapel Hill, NC 27599, USA
6. Department of Bionanoscience, Kavli Institute of Nanoscience, Delft University of Technology, Van der Maasweg 9, 2629 HZ Delft, the Netherlands

*These authors contributed equally to the present work.

To Whom the correspondence must be addressed: d.dulin@vu.nl; s.m.depken@tudelft.nl.

Abstract

The genome of most positive-sense (+)RNA viruses encodes a helicase, such as the coronavirus (CoV) nsp13-helicase, but little is known about their actual function, despite being absolutely essential for CoV replication. The CoV polymerase associates with two nsp13-helicases, which translocates in the opposite direction, raising questions about nsp13-helicase role during viral RNA synthesis. Using magnetic tweezers, we show that nsp13-helicase specifically associates with the CoV polymerase and tranlocates on the strand opposite to the template, increasing the overall RNA synthesis rate on a double-stranded (ds) RNA template by ten-fold. Nsp13-helicase utilizes both ATP hydrolysis and allostery to assist the CoV polymerase through the dsRNA fork. Our kinetic modelling provides the energy landscape of the two nsp13-helicases association with the polymerase and describes the nucleotide addition mechanochemistry of the resulting complex. Our study demonstrates a new function for (+)RNA virus helicase and deepens the understanding of CoV replication and transcription.

Introduction

Most (+)RNA viruses encode a helicase in their genome, e.g. flaviviridae NS3 (e.g. hepatitis C, dengue) and alphavirus nsP2 and the coronavirus non-structural protein (nsp) 13 (*1, 2*), all belonging to either the super family 1 or 2 (*3*). They are monomeric helicases that use ATP hydrolysis to translocate on single-stranded (ss) and unwind double-stranded (ds) nucleic acids, and have been proposed to support viral RNA synthesis by associating with the viral RNA-dependent RNA polymerase (RdRp) (*3*). While NS3 helicases exhibit a 3' to 5' polarity, i.e. matching their RdRp, alphavirus nsP2 and coronavirus nsp13 helicases display a 5' to 3' polarity, i.e. opposite to their RdRp, raising questions about the mechanism by which those helicases may support replication. Recent cryo-electron microscopy (EM) studies have revealed the architecture of the helicases-polymerase complex for dengue virus, chikungunya virus and SARS-CoV-2 (*4-6*). However, functional studies demonstrating their active role during RNA synthesis are still lacking.

Here, we focus on the SARS-CoV-2 replication-transcription complex (RTC), for which exists an extensive structural knowledge as a result of the COVID-19 pandemic (*7*). The RTC is constituted of a core, i.e. nsp12-polymerase, nsp7 and nsp8 in a 1:1:2 stoichiometry (**Fig. 1A**) (*8-10*), to which associates two nsp13-helicases, i.e. nsp13.1 and nsp13.2 (**Fig. 1A**) (*4, 11, 12*). Nsp13-helicase has the typical structure of the super family 1B helicases, with two RecA domains (RecA1 and RecA2) sandwiching an ATP binding site and a single-stranded nucleic acid binding groove formed by the RecA domains on one side and the 1B and stalk domains on the other side (**Fig. 1A**) (*13*). Single-molecule studies have reported rapid and processive dsRNA unwinding by nsp13-helicase when mechanically assisted (*14, 15*). Cryo-electron microscopy (EM) studies have reported that only nsp13.1 bound to RNA, i.e. the template strand (**Fig. 1A**), but not nsp13.2 (*4, 11*). Nsp13.1 has therefore been proposed to be involved in RTC backtracking, a possible intermediate in sub-genomic RNA synthesis, viral RNA recombination and proofreading (*4*). On the other hand, no specific function has been attributed to nsp13.2, apart from allosterically controlling the productive engagement of nsp13.1 with the template RNA (*16*). Downstream duplex RNA represents a mechanical barrier to the elongating SARS-CoV-2 core RTC, resulting in an increased probability of long-lived pauses, resulting in a very slow RNA synthesis (*17*). This suggests that one of the two nsp13-helicases may be actively supporting the CoV RTC during viral RNA synthesis through structured RNA (*18*), though such a function has never been demonstrated.

We employed high-throughput magnetic tweezers to investigate how nsp13-helicase associates with the CoV RTC and impacts the dynamics of RNA synthesis. We show that nsp13-helicase specifically

associates with the elongating core RTC and not with the polymerase freely diffusing in solution, and that nsp13.2 enables rapid RNA synthesis through long dsRNA by translocating on the strand opposite to the template, i.e. the non-template strand. We show that three different complexes, populated as a function of nsp13-helicase concentration, are capable of RNA synthesis and co-exist at equilibrium: the core RTC alone, the core RTC associated with nsp13.1 and the core RTC associated with nsp13.1 and nsp13.2. The latter complex exists in two modes, i.e. either non-engaged or engaged with the non-template RNA, and only the engaged mode enables very fast RTC elongation through nsp13-helicase ATPase activity. Furthermore, a mechanochemical analysis of the data shows that nsp13.2 also increases the average elongation rate by allostery upon association with the RTC. Our assay demonstrates a new role for (+)RNA virus helicases, opening new avenues to investigate polymerase-helicase coupling of other (+)RNA virus families.

Results

Nsp13-helicase promotes rapid RNA synthesis on a dsRNA template by the CoV RTC.

We employed a high-throughput magnetic tweezers assay to monitor CoV RTC elongation on dsRNA, as previously described for poliovirus (PV) RdRp (*19, 20*). In short, a pair of permanent magnets located above a flow chamber is used to apply an attractive force to the magnetic beads tethered to the glass surface of a flow chamber by a ~3.2 kbp dsRNA construct (**Fig. 1A, Materials and Methods**) (*21*). After flushing the reaction buffer containing the viral proteins and NTP (**Materials and Methods**), the RTC assembled on a small hairpin terminating the template strand 3'-end and elongated through the dsRNA until reaching the end of the 2820 nt long template strand (**Fig. 1B**). The RTC elongation activity converted the dsRNA tether into ssRNA, resulting in an increase of the tether extension (**Fig. 1B**) (*22*). The force was kept constant throughout the experiment by maintaining the magnets-magnetic bead distance constant (*23, 24*). In absence of nsp13-helicase, we found that the core RTC elongates slowly on dsRNA, with an average velocity of $(3.6 \pm 0.1)\ \mathrm{nt}/s$ (**Fig. 1CE**). Adding 50 nM of nsp13-helicase to the reaction buffer dramatically increased the average elongation velocity to $(27.9 \pm 2.6)\ \mathrm{nt}/s$ (**Fig. 1CE**), showing that nsp13-helicase supports RNA synthesis through duplex RNA. Decreasing nsp13-helicase concentration to 3 nM, we could distinguish very fast nucleotide addition bursts of tens to hundreds of nucleotides, interrupted by slow nucleotide addition activity (**Fig. 1E**). Varying the concentration of nsp13-helicase from 0 to 50 nM, we clearly observed an increase in the average elongation velocity, until saturating above 10 nM (**Fig. 1E**), indicating that nsp13-helicase association with the elongating RTC is a dynamic equilibrium. Interestingly, the saturating concentration of nsp13-helicase is to be compared with nsp12-polymerase concentration, i.e. 200 nM, indicating that nsp13-helicase binds the elongating core RTC with a much higher affinity than freely diffusing nsp12-polymerase or core RTC. This likely originates from

nsp13.1 and nsp13.2 forming interactions and nsp8.2 and nsp8.1 N-terminal poles (**Fig. 1A**), respectively (*4, 11*). Indeed, these poles are very flexible in absence of duplex RNA (*9, 25*), which may hinder nsp13-helicase association.

Nsp13-helicase specifically associates with the CoV core RTC and translocates on the non-template RNA strand.

We then investigated whether nsp13-helicase associates specifically with the core RTC and how it increases RNA synthesis rate. We replaced the core RTC by the poliovirus RdRp, which can employ the same dsRNA template (*19*). As poliovirus RdRp has a different structure from the CoV core RTC (*9*), we hypothesized that no specific interaction could form between poliovirus RdRp and nsp13-helicase. Indeed, monitoring poliovirus RdRp elongation dynamics either with or without nsp13-helicase, we observed no significant difference in the traces between the two experiments, with respective average elongation velocities of (19.3 ± 0.4) nt$/s$ and (19.9 ± 0.4) nt$/s$ (**Fig. 2A**, **Fig. S3ACD**). To further interrogate the specificity of nsp13-helicase association, we monitored the core RTC elongation dynamics in the presence of the ATPase-dead mutant K288A nsp13-helicase (**Fig. 2B**). A significant reduction of the RTC average elongation velocity relative to the core RTC alone was noticeable, i.e. (1.1 ± 0.1) nt$/s$ vs. (3.7 ± 0.1) nt$/s$, originating from an increase of the long-lived pause probability (**Fig 2B**, **Fig. S3BCD**). We concluded from these experiments that nsp13-helicase forms a specific complex with the core RTC and that removing nsp13-helicase ATPase activity further impairs the RTC elongation through dsRNA.

We then employed an ssRNA template to investigate whether nsp13-helicase impacts the elongation activity of the core RTC in absence of a complementary strand annealed to the template. Nsp13-helicase translocates very fast from 5' to 3', ~1 kb/s on ssRNA (*26*), while the elongating core RTC is much slower, ~50 nt/s (*17*), suggesting that head-to-head collisions of nsp13-helicase and the RTC may occur in such configuration. We employed a ~1 kb long ssRNA template to monitor the RTC primer-extension dynamics (*17, 27*) at increasing concentrations of nsp13-helicase (**Fig. 2C**). When comparing the cases with or without 20 nM nsp13-helicase, we observed neither a decrease in product length, i.e. (939 ± 22) nt and (983 ± 36) nt, respectively, nor a slowdown in the RTC average elongation velocity (**Fig. 2C**). On the contrary, we monitored a small, but significant, increase in the average elongation velocity, i.e. (67.2 ± 1.4) nt$/s$ with respect to (51.5 ± 1.1) nt$/s$ without nsp13-helicase, indicating that nsp13-helicase allosterically increases the elongation rate after binding the core RTC. If collisions between translocating nsp13-helicase and RTC occurred, they did not significantly impact the elongation of the latter. In summary, we only observed burst of rapid RNA synthesis by the RTC with active nsp13-helicase on a dsRNA template, while we obtained much slower elongation dynamics in presence of the ATPase dead mutant

K288A, indicating that nsp13-helicase associates with the non-template strand to support RTC elongation. As nsp13.1 has been shown to be in association with the template strand (*4, 28*), we conclude that nsp13.2 supports RTC elongation by translocating on the non-template strand (**Fig. 2D**).

In the following sections, we will employ these observations, together with a dwell-time analysis and modeling, to describe the mechanism and the energy landscape of the association of two nsp13-helicases with the core RTC (**Fig. 3**). Furthermore, we will describe how nsp13-helicase association affects the nucleotide addition cycle of nsp12-polymerase (**Fig. 4**).

Nsp13-helicase modifies the kinetic fingerprint of the RTC elongation traces

To understand the mechanism of assembly of nsp13-helicase with the core RTC, we analyzed the RTC elongation dynamics on a dsRNA template as a function of nsp13-helicase concentration (**Fig. 1C-E**). To this end, we performed a dwell-time analysis, i.e. we scanned the elongation traces with a non-overlapping ten nucleotides window and measure the duration of ten consecutive nucleotide addition cycles, which we coined dwell-times (*22, 29*). The dwell-times were assembled into distributions, which were fitted with a dwell-time fit-function using a maximum likelihood estimation approach to extract the characteristic timescales and probabilities of the underlying probability density functions (**Fig. 3AB**, **Materials and Methods**, **Supplementary Information Section S1**) (*29*). The dwell-times are a representation of the kinetic event that dominates the ten consecutive nucleotide additions. We previously showed that there are four of these events for the core RTC elongation dynamics described by four probability density functions combined into one dwell-time fit-function (*17*). For the shortest dwell-times we fitted a gamma distribution representing the ten uninterrupted, fast nucleotide additions (FNA). Then we have two exponential distributions for dwell-times of a duration from 1 to 20 s which describe either a slow or a very slow nucleotide addition cycle (SNA and VSNA, respectively) within the ten consecutive nucleotide additions. Finally, a power law distribution with a $t^{-3/2}$ decay describes the dwell-times longer than ~20 s (**Fig. 3AB**). These long dwell-times are dominated by a slow RTC-RNA conformational change described by a one-dimensional diffusion in a periodical energy landscape (*30*), such as SARS-CoV-2 core RTC backtracking (*17*). Theoretical analysis of the $t^{-3/2}$ decay shows that the period in the energy landscape should be smaller than 0.02, i.e. much smaller than a dsRNA base pair (**Supplementary Information Section S1**). This indicates that the long-lived pauses depict slow and non-catalytic events, such as polymerase backtracking (*17*) or slow RTC domain reconfiguration (*31*). For now, we will refer to these slow events as long-lived pauses. Importantly, in the presence of nsp13-helicase, a new gamma distribution appeared on the left-hand side of the dwell-time distribution (**Fig. 3AB**), describing the very fast nucleotide addition (VFNA) bursts observed in the traces (**Fig. 1D**). The combined fit-function captures well the characteristic trends in the

dwell-time distributions for all conditions tested for the core RTC with different concentrations of nsp13-helicase in the reaction mixture (**Fig. S8**). Interestingly, we note that the population of the VFNA gamma distributions grows (moves upward) while the other distributions diminish (move downward) for increasing nsp13-helicase concentration (**Fig. 3A**). In conclusion, the dwell-time analysis reports on four nucleotide addition pathways in presence of nsp13-helicase, i.e. VFNA, FNA, SNA, VSNA, and non-catalytic long-lived pauses.

An assembly model of nsp13-helicase to the core RTC.

We observed that the VFNA bursts lasted tens to hundreds of nucleotide addition cycles without interruption, i.e. without entering FNA, SNA, VSNA or long-lived pauses, even at low nsp13-helicase concentration (**Fig. 1D**). Furthermore, we noticed that the characteristic timescale of the VFNA pathway is independent of nsp13-helicase concentration (**Fig. 3D**, **Fig. S2AI**). Both observations suggest that a single complex is responsible for the VFNA pathway and is stable over multiple dwell-time windows. Either nsp13.1 or nsp13.1 and nsp13.2 are associated with the core RTC, but never with nsp13.2 alone (*4, 11*), suggesting a stepwise assembly process, where nsp13.1 binds the core RTC first, followed by nsp13.2.

The dwell-time distributions representing the RTC-elongation dynamics on dsRNA saturated at nsp13-helicase concentrations above 10 nM, indicating that the association of the two nsp13-helicases to the RTC is equilibrated at these concentrations (**Fig. 3A**). However, we still observed slow kinetic events in those traces (**Fig. 1C**). Indeed, the FNA, SNA, VSNA pathways and the long-lived pause are still populated in the dwell-time distribution at saturating nsp13-helicase concentration (**Fig. 3A**). The dwell-time fits further support these observations. Indeed, the VFNA probability increased with nsp13-helicase concentration, while the FNA and SNA characteristic timescales (**Fig. 3C**) and the FNA, SNA, VSNA and long-lived pause probabilities (**Fig. 3D**) significantly decreased and saturated for nsp13-helicase concentrations above 10 nM. Therefore, two states of the RTC with two nsp13-helicases co-exist, i.e. one entering the VFNA pathway only and one entering the FNA, SNA, VSNA pathways and the long-lived pause (**Fig. 3BCD**, **Fig. S6**). Nsp13.2 has been shown to allosterically control the productive engagement of nsp13.1 with the RNA template strand (*16*). Here, we hypothesized that the reciprocal is also true, i.e. nsp13.1 allosterically controls the engagement of nsp13.2 with the non-template RNA strand, meaning that only one of the two helicases can be productively engaged with their respective RNA at a time. Therefore, there are two populations of RTC with two helicases bound, one with nsp13.2 engaged with the non-template RNA (VFNA pathway) and one with nsp13.2 non-engaged (core RTC-like elongation dynamics).

Additionally, we observed a significant decrease in the FNA and SNA characteristic timescale for RTC elongation on the dsRNA template, which saturates above 10 nM nsp13-helicase (**Fig. 3C**). This is supported by a decrease observed in the FNA characteristic timescale for RTC elongation on ssRNA saturating only for high nsp13-helicase concentration (20 nM) (**Fig. S5**), indicating that the effect results from nsp13.2 association and impacts RTC-nsp13.1,2 elongation dynamics. Furthermore, in presence of saturating concentration of ATPase-dead nsp13-helicase (20 nM) we observed a significant decrease in the FNA characteristic timescale, resulting from allostery, concomitant to an increase in the timescales and probabilities of the slower pathways (SNA, VSNA and LLP) (**Fig. S5**).

Based on these findings, we derived an assembly model where nsp13.1 binds first to the core RTC (RTC-nsp13.1), followed by nsp13.2 (RTC-nsp13.1,2), which can then engage with the non-template RNA strand (RTC-nsp13.1,2*), resulting in the very fast nucleotide addition (VFNA) bursts (**Fig. 3E, Fig. S4**, **Supplementary Information Section S2**). Furthermore, the elongation dynamics of the core RTC and RTC-nsp13.1 are indistinguishable, while RTC-nsp13.1,2 employs the same pathways as the core RTC but with different timescales and probabilities due to allostery (**Fig. S9-S13**, **Table S2, Supplementary Information Section S2**) and RTC-nsp13.1,2* enters only the VFNA pathway (**Fig. S6**). The concise RTC assembly-RNA synthesis dynamics model was globally fitted to the dwell-time distributions obtained at nsp13-helicase concentrations varying from 0 to 50 nM (solid lines, **Fig. 3DE**, **Fig. S10**), and was in good agreement with the parameters extracted from the dwell-time fits (circles, **Fig. 3DE**).

We extracted the free energy difference between the core RTC and each RTC complex associated with nsp13-helicase (**Fig. 3E**), i.e. $(1.5 \pm 0.3)\ k_BT$ for RTC-nsp13.1, $(0.8 \pm 0.2)\ k_BT$ for RTC-nsp13.1,2 and $(-0.7 \pm 0.0)\ k_BT$ for RTC-nsp13.1,2*, respectively. From these free energy differences, we derived the fractional occupancy of each complex, i.e. (0.65±0.01) for RTC-nsp13.1,2*, (0.31±0.01) for RTC-nsp13.1,2, (0.035±0.007) for RTC-nsp13.1 and (0.0079±0.0008) for the core RTC at 20 nM nsp13-helicase (saturating concentration) (**Fig. 3F**), and the equilibrium association constants K_a for the binding of nsp13.1 to the RTC and for nsp13.2, i.e. (0.23±0.07) nM^{-1} and (0.46±0.10) nM^{-1}, respectively (**Materials and Methods**).

The CoV RTC nucleotide addition cycle.

To build a mechanochemical model that captures the interrelated trends of the different pathways, we start with a model where the NA cycle includes translocation, nucleotide binding, catalysis, and pyrophosphate release (**Fig. S7A**). Each NA cycle starts with the RTC in the pre-translocated state. From

there, the RTC translocates forward, and thereafter binds an NTP, where both the translocation and NTP binding steps are reversible and may occur several times before chemistry (**Fig. S7A**).

We then set out to characterize the mechanochemistry of the nucleotide addition cycle of a CoV RTC elongating on a dsRNA template, either without (**Fig. 4ACE**) or with nsp13-helicase at saturating concentration (20 nM) (**Fig. 4BDF**). In the latter case, we considered only two RTCs, i.e. RTC-nsp13.1,2 and RTC-nsp13.1,2* in our model, as they dominate the RTC population at saturating nsp13-helicase concentration (**Fig. 3G**). We performed RTC elongation experiments at increasing RNA tension, which destabilizes the replication fork and thus decreases the bias towards the pre-translocated state (**Fig. 1B**) (*20, 22*). We considered that the FNA, SNA and VSNA pathways are parallel nucleotide addition pathways (**Fig. 4G**, **Fig. S7A**) (*17*). We observed that the average elongation velocity of the core RTC on dsRNA is significantly lower than on ssRNA, i.e. (3.6 ± 0.1) nt/s vs. (51.5 ± 1.1) nt/s), respectively, indicating that translocation is rate-limiting on dsRNA. We therefore assumed that NTP (un)binding was very fast with respect to translocation and thus in rapid equilibrium, giving an effective rate of nucleotide addition.

We then investigated how the different nucleotide addition pathways are linked for the core RTC and non-engaged RTC-nsp13 complexes, assuming that the existence and interconnection of the pathways does not depend on the presence of nsp13-helicase (*17*). To this end, we inspected how the dwell-time fit parameters changed as a function of applied tension (circles, **Fig. 4C-F**). For the slow nucleotide addition pathways, i.e. FNA, SNA and VSNA, we noted that the FNA characteristic timescale of the core RTC decreased with increasing RNA tension, indicating that the tension biased the RTC towards the FNA post-translocated state. Furthermore, the FNA probability increased with tension while the SNA and VSNA probability decreased (circles, **Fig. 4E**), suggesting that the slower NA pathways originate from the pre-translocated state of the FNA pathway (**Fig. S7B**, **Supplementary Information Section S3**). We already reported this behavior for the core RTC (*17*), though not the order of entry. We observed that the SNA probability becomes relatively higher than the VSNA probability when increasing tension (**Fig. 4E**), indicating that the VSNA pathway is entered from the SNA pre-translocated state (**Fig. S7B**). The long-lived pause probability shows similar tension dependent trends as the VSNA probability (**Fig. 4EF**), suggesting that it is also entered from the pre-translocated state. For simplicity, we consider the long-lived pause is entered from the pre-translocated state of each NA pathway with a constant relative rate (**Fig. 4G**).

The VFNA probability is not dependent on RNA tension, indicating that the stability of the RTC-nsp13.1,2* complex is not impacted by increasing the tension. Furthermore, the characteristic timescale of the bursting NA pathway (VFNA) shows no significant trends with tension (**Fig. 4DF**) and is therefore rate-limited by a tension-independent step. The VFNA pathway is still significantly slower (~50 nt/s) (**Fig. 4D**)

than the FNA pathway observed on ssRNA in similar conditions (~90 nt/s) (**Fig. S5**), indicating that translocation is still dominating the VFNA characteristic timescale.

We conclude that the nucleotide addition cycle starts in the pre-translocated state of the FNA pathway. From there, the complex can either directly incorporate a nucleotide or enter the SNA pre-translocated state, then either incorporate a nucleotide via the SNA or enter the VSNA pre-translocated state and incorporate a nucleotide. The long-lived pauses can be entered from the pre-translocated state of all the pathways but the VFNA. Finally, the RTC-nsp13.1,2* complex incorporates nucleotides only via the VFNA pathway.

Allosteric effect from nsp13.2 association on RTC-nsp13.1,2 nucleotide addition cycle mechanochemistry.

We can now describe how nsp13.2 association with the RTC allosterically increases RTC-nsp13.1,2 elongation velocity (**Fig. 2C**, **Fig. 3CD**, **Fig. S5**, **Supplementary Information Section S2**), and which steps in the mechanochemical model are affected. As mentioned before, we assume the general reaction scheme is not affected by nsp13-helicase binding (**Fig. 4G**), but that the rates changed. Increasing the RNA tension had no significant effect on the FNA characteristic timescale and probability of RTC-nsp13.1,2 (**Fig. 4DF**), indicating that the FNA backward translocation rate is negligible for this complex (**Table S3**, **Supplementary Information Section S3**). On the other hand, we observed that the SNA characteristic timescale decreased with RNA tension for both the core RTC and RTC-nsp13.1,2, although with a lower starting point at 20 pN (**Fig. 4D**). This indicates that the cycle of backward and forward translocation are not completely abolished for the SNA pathway by RTC-nsp13.1,2 and the backward translocation rate is reduced but not negligible (**Table S3**). Interestingly, the VSNA probability decreased much more than the SNA and long-lived pause probabilities (**Fig. 3D, Fig. 4EF**, **Table S3**), i.e. the probability to reach the chemistry step in the VSNA pathway is decreased for the RTC-nsp13.1,2 complex.

In conclusion, nsp13.2 association to the RTC allosterically promotes forward over backward translocation and makes backward translocation negligible in the FNA pathway specifically. The allosteric effect also reduced the backward translocation rate in the SNA pathway. Additionally, the probability to reach the chemistry step in the VSNA pathway decreases for RTC-nsp13.1,2.

A mechanochemical model for the nucleotide addition cycle of the CoV RTC in association with nsp13-helicase.

Combining the mechanochemical model with the RTC assembly - Elongation dynamics model, as illustrated in **Fig. S1**, we performed a global fit on the nsp13-helicase concentration and tension dependency data (solid lines in **Fig. 3CD** and **Fig. 4C-F**, **Fig. S14**, **Materials and Methods, Supplementary Information Section S3**). The global fit of the RTC assembly - Elongation dynamics model and the mechanochemical model (solid lines, **Fig. 3CD** and **Fig. 4C-F**) captures well all the trends extracted from the individual dwell-time fits (circles, **Fig. 3CD** and **Fig. 4C-F**). We extracted the kinetic rates represented in **Fig. 4G** from the global fit (**Table S3**), which we will discuss and put into perspective. The core RTC and RTC-nsp13.1 have indiscernible elongation dynamics (**Fig. S6**), therefore the same rates in the mechanochemical model, and we thereafter refer only to the core RTC. We are now comparing the kinetics rates extracted from the global fit for the core RTC and RTC-nsp13.1,2 for each nucleotide addition pathway.

Starting with the FNA pathway, we measured for the core RTC a forward translocation rate ~2.5-fold smaller than the backward translocation rate, i.e. $k_{\mathrm{post}}^{\mathrm{FNA}} = (108 \pm 6)\ s^{-1}$ vs. $k_{\mathrm{pre}}^{\mathrm{FNA}} = (269 \pm 23)\ s^{-1}$, respectively, resulting in a more populated pre-translocated state than the post-translocated state. The entrance rates for the SNA pathway and the long-lived pauses are $k_{\mathrm{in}}^{\mathrm{SNA}} = (3.9 \pm 0.1)\ s^{-1}$ and $k_{\mathrm{in}}^{\mathrm{LLP}} = (0.013 \pm 0.006)\ s^{-1}$, respectively, i.e. ~30- and ~8000-fold smaller than the FNA forward translocation rate, and ~10- and ~3000-fold smaller than the combined NTP binding and catalysis rate of the FNA pathway ($k_{\mathrm{irr}}^{\mathrm{FNA}} = (39.9 \pm 0.4)\ s^{-1}$), resulting in the FNA pathway being more populated than the slower pathways (**Fig. 4E**). For RTC-nsp13.1,2, we measured a ~7-fold decrease of the FNA backward translocation rate $k_{\mathrm{pre}}^{\mathrm{FNA}}$ from $(269 \pm 23)\ s^{-1}$ to $(39.4 \pm 8.7)\ s^{-1}$, originating from allostery, while the FNA forward translocation rate $k_{\mathrm{post}}^{\mathrm{FNA}}$ remained unchanged. As a consequence, the RTC-nsp13.1,2 FNA pathway has a characteristic timescale shorter than for the core RTC, and is therefore relatively more populated (**Fig. 4D, Table S3**).

Concerning the SNA pathway, we observed that the forward translocation rate is ~100-fold slower than the backward translocation rate for the core RTC, i.e. $k_{\mathrm{post}}^{\mathrm{SNA}} = (96 \pm 11)\ s^{-1}$ vs. $k_{\mathrm{pre}}^{\mathrm{SNA}} = (10191 \pm 1147)\ s^{-1}$. For the core RTC, the SNA pre-translocated state is therefore much more populated than its SNA post-translocated state. Since the entrance rates of the VSNA pathway and the long-lived pauses are ~700- and ~7000-fold smaller than the SNA forward translocation rate ($k_{\mathrm{in}}^{\mathrm{VSNA}} = (0.14 \pm 0.01)\ s^{-1}$ and $k_{\mathrm{in}}^{\mathrm{LLP}} = (0.013 \pm 0.006)\ s^{-1}$) and are ~140- and ~1500-fold smaller than the

combined rate of NTP binding and catalysis ($k_{\mathrm{irr}}^{\mathrm{SNA}} = (20.0 \pm 0.4)\ s^{-1}$), the probability to exit through the SNA pathway is therefore much larger than the probability to enter either the VSNA pathway or the long-lived pauses (**Fig. 4CE**). For RTC-nsp13.1,2, the SNA backward translocation rate is reduced with respect to the core RTC, but $k_{\mathrm{pre}}^{\mathrm{SNA}}$ is still ~40-fold larger than the SNA forward translocation rate $k_{\mathrm{post}}^{\mathrm{SNA}}$, which remains unchanged. As a result, the SNA characteristic timescale still shows a significant tension dependency for RTC-nsp13.1,2 (**Fig. 4D**) and the probabilities to enter the VSNA pathway and the long-lived pauses decrease with increasing RNA tension (**Fig. 4F**, **Table S3**).

Since we did not observe any significant trend in the VSNA characteristic timescale (**Supplementary Information Section S1**), we could only extract the probability $p_{\mathrm{irr}}^{\mathrm{VSNA}}$ for the irreversible step of the VSNA pathway starting from the VSNA pre-translocated state, which competes with the entrance rate of the long-lived pauses (**Fig. 4G**). This probability significantly decreases from the core RTC (0.92 ± 0.05) to the RTC-nsp13.1,2 complex (0.05 ± 0.03), resulting in a much lower VSNA probability compared to the other pathways (**Fig. 4F**, **Table S3**).

Discussion

While nsp13-helicase has been proposed to support RNA synthesis (*12*), this function remained to be shown. Here, we employed a high-throughput, single-molecule, magnetic tweezers assay to show that nsp13-helicase specifically associates with the elongating core RTC and that nsp13.2 supports RTC elongation on a dsRNA template by translocating on the non-template strand (**Fig. 1**, **Fig. 2**). These results solve the conundrum of opposite polarity between nsp13-helicase and nsp12-polymerase. The large statistics acquired for many conditions enabled the application of an extensive statistical analysis and theoretical modeling, revealing the mechanism of assembly of the CoV RTC, with the two nsp13-helicases associating sequentially to the core RTC, i.e. nsp13.1 binding first, followed by nsp13.2 (**Fig. 2**, **Fig. 3**). Furthermore, our data support a model where nsp13.2 alternates between a non-engaged and an engaged state with the non-template RNA, which are respectively responsible for ~35% and ~65% of the incorporated nucleotides at saturating nsp13-helicase concentration, i.e. above 10 nM (**Fig. 3**). Finally, we derived a mechanochemical model describing how nsp13.2 supports elongation, i.e. either actively (RTC-nsp13.1,2*) by engaging with the non-template RNA and ATP-hydrolysis (VFNA pathway), or allosterically (RTC-nsp13.1,2) by biasing nsp12-polymerase towards the post-translocated state (**Fig. 4**).

Our data supports a model where nsp13.2 assists the CoV RTC elongation dynamics through long dsRNA and nsp13.1 allosterically controls nsp13.2 productive engagement with the non-template RNA, similarly to nsp13.2 controlling nsp13.1 productive engagement with the template RNA (*16*). We propose that this mechanism ensures only one helicase at a time is actively engaged with its associated RNA strand, preventing antagonistic activities. Nsp13.1 has been proposed to stimulate RTC backtracking, to promote either polymerase strand switching (*7*) or proofreading by nsp14-ExoN (*4*), though both of these functions remains to be demonstrated (*12*). However, when nsp13.2 is engaged, the RTC only perform very fast nucleotide addition, and therefore only a non-engaged nsp13.2 would enable entry into a backtrack state. Remarkably, at saturating nsp13-helicase concentration, the RTC stochastically enters the slower pathways in ~15% of the nucleotide addition cycles (**Fig. 3F**), which may help regulating nsp13.1 productive engagement with the template RNA, and thereby entry of the long-lived pause. This ability to stochastically switch between nsp13.1 and nsp13.2 productive engagement may enable a higher level of regulation of replication and transcription in CoV, such as to sense a specific sequence in the CoV genome like the transcription regulatory sequences (TRS) or a nucleotide mismatch incorporation. Future studies will investigate these different activities of nsp13-helicase within the CoV RTC in greater detail, and how other nsp's may further modulate nsp13-helicase activity and CoV RNA synthesis.

We anticipate that our results will impact our understanding of the mechanism of action of antiviral nucleotide analogs targeting nsp12-polymerase, such as the FDA approved remdesivir (*32*) and molnupiravir (*33*). Indeed, remdesivir incorporation by nsp12-polymerase has been shown to induce RTC long-lived pauses during elongation (*27*), originating from a steric clash between remdesivir and nsp12-polymerase serine 861 (*34-37*). As nsp13.2 assists the RTC to elongate through dsRNA, it is tempting to think that nsp13-helicase may help reducing the duration of the pause induced by remdesivir incorporation. Future studies will investigate how the mechanism of action of antiviral nucleoside analogs targeting the CoV RTC should be revised when evaluated in the presence of nsp13-helicase.

Our approach combining high-throughput single-molecule biophysics and advanced theoretical modeling is uniquely capable of reconstituting an RNA synthesis-competent extended CoV RTC, greatly complementing our structural knowledge with function. This study paves the way towards the investigation of other (+)RNA virus RTC and reveal whether the function discovered here for CoV nsp13-helicase is conserved for helicases from different (+)RNA virus families.

Supplemental information

Supplemental Information can be found online.

Acknowledgements

DD was supported by the Interdisciplinary Center for Clinical Research (IZKF) at the University Hospital of the University of Erlangen-Nuremberg, BaSyC – Building a Synthetic Cell" Gravitation grant (024.003.019) of the Netherlands Ministry of Education, Culture and Science (OCW) and the Netherlands Organisation for Scientific Research (NWO), and NWO funding OCENW.XL21.XL21.115. DD, JJA and CEC were supported from grant R01 AI161841-01 and U19 AI171292 from NIAID, NIH. RNK was supported by grant AI158463 from NIAID, NIH. KDR was supported by NIGMS funding R35-GM12260. DD thanks Nico van der Vis for his help for data acquisition.

Authors contribution

DD, KDR, CEC and JJA designed the research. DD and SCB designed the experiments. SCB and AD performed the experiments. SCB and PPBA analyzed the data. FSP made the RNA construct used for the study. TKA and RNK provided SARS-CoV-2 core RTC proteins. JJA and CEC provided poliovirus proteins. KDR and JCM provided the coronavirus nsp13-helicase. PPBA and MD developed the theoretical modeling. PPBA, MD and DD interpreted the results. PPBA and DD wrote the article. DD supervised the research. All authors have edited the manuscript.

Declaration of interests

The authors declare no competing interest.

Materials and Methods

Recombinant Protein Expression of RdRp (nsp12) and cofactors (nsp7 and nsp8) from SARS-CoV-2.

This protocol was described in Ref. (*27*). The SARS-CoV-2 nsp12 gene was codon optimized and cloned into pFastBac with C-terminal additions of a TEV site and strep tag (Genscript). The pFastBac plasmid and DH10Bac E. coli (Life Technologies) were used to create recombinant bacmids. The bacmid was transfected into Sf9 cells (Expression Systems) with Cellfectin II (Life Technologies) to generate recombinant baculovirus. The baculovirus was amplified through two passages in Sf9 cells, and then used to infect 1 L of Sf21 cells (Expression Systems) and incubated for 48 hrs at 27°C. Cells were harvested by centrifugation, resuspended in wash buffer (25 mM HEPES pH 7.4, 300 mM NaCl, 1 mM $MgCl_2$, 5 mM DTT) with 143 µl of BioLock per liter of culture. Cells were lysed via microfluidization (Microfluidics). Lysates were cleared by centrifugation and filtration. The protein was purified using StrepTactin Superflow agarose (IBA). StrepTactin eluted protein was further purified by size exclusion chromatography using a Superdex 200 Increase 10/300 column (GE Life Sciences) in 25 mM HEPES, 300 mM NaCl, 100 µM $MgCl_2$, 2 mM TCEP, at pH 7.4. Pure protein was concentrated by ultrafiltration prior to flash freezing in liquid nitrogen. The SARS-CoV-2 nsp7 and nsp8 genes were codon optimized and cloned into pET46 (Novagen) with an N-terminal 6x histidine tag, an enterokinase site, and a TEV protease site. Rosetta2 pLys E. coli cells (Novagen) were used for bacterial expression. Cultures were grown to an OD600 of 0.8 and induced with a final concentration of 0.5 mM isopropyl β-D-1-thiogalactopyranoside (IPTG) and growth temperature was reduced to 16°C for 16 hrs. Cells were harvested by centrifugation and pellets were resuspended in wash buffer (10 mM Tris pH 8.0, 300 mM NaCl, 30 mM imidazole, 2 mM DTT). Cells were lysed via microfluidization and lysates were cleared by centrifugation and filtration. Proteins were purified using Ni-NTA agarose beads (Qiagen) and eluted with wash buffer containing 300 mM imidazole. Eluted proteins were digested with 1% w/w TEV protease during overnight room temperature dialysis (10 mM Tris pH 8.0, 300 mM NaCl, 2 mM DTT). Digested proteins were passed back over Ni-NTA to remove undigested protein before concentrating the proteins by ultrafiltration. Nsp7 and nsp8 proteins were further purified by size exclusion chromatography using a Superdex 200 Increase 10/300 column (GE Life Sciences). Purified proteins were concentrated by ultrafiltration prior to flash freezing with liquid nitrogen.

Recombinant Protein Expression of the wild-type and the ATPase dead mutant K288A nsp13-helicases from SARS-CoV-2.

The coding sequence for nsp13-helicase from the SARS CoV-2 Washington isolate (Genbank MN985325) was synthesized as an *E. coli* codon-optimized fragment (GenScript, Piscataway NJ) and cloned into the *Bsa*I site of the pSUMO plasmid (LifeSensors, Malvern, PA) to produce an *N*-terminal six histidine-tagged

SUMO-NSP13-HELICASE fusion cassette (6XHis-SUMO-nsp13). Using the manufacturer's recommendations (QuikChange II Site-Directed Mutagenesis Kit, Agilent Technologies), oligonucleotide-directed site-directed mutagenesis was used to mutate the codon in the wild type nsp13-helicase for the critical catalytic lysine in the Walker A motif (K288) to an alanine residue. This change produced the K288A mutant lacking ATPase activity (designated nsp13D). Final wild-type and mutant plasmids were sequence-verified through the UAMS Sequencing Core Facility using a 3130XL Genetic Analyzer (Applied Biosystems, Foster City, CA). The SUMO-nsp13 and the SUMO-nsp13D constructs were transformed into Rosetta2 cells, and colonies were grown overnight at 37°C in NZCYM (Research Products International, Mount Prospect, IL) supplemented with kanamycin (50 µg/ml) and chloramphenicol (25 µg/ml). The cultures were diluted 1:100 into fresh antibiotic-containing NZCYM media and grown to an $OD_{600\ nm}$ of 0.8-1. The bacterial media was supplemented with 0.1 mM $ZnSO_4$ and 0.2% dextrose and cooled on ice for 10 min. Wild type and mutant protein expression was induced with 0.2 mM isopropyl β-D-1-thiogalactopyranoside (IPTG) at 18°C for 12-16 hours. The cells were harvested by centrifugation at 4,000 x *g* for 15 min at 4°C, and pellets stored at -80°C.All purifications steps were carried out on ice or at 4°C. Pellets were resuspended in lysis buffer (50 mM sodium phosphate, pH 8.0, 300 mM NaCl, 1 mM β-mercaptoethanol, 10% glycerol and 20 mM imidazole) supplemented with 2 mM phenylmethylsulfonyl fluoride (PMSF) and 1X EDTA-free protease inhibitor cocktail (Pierce). Bacteria were lysed by microfluidization and the lysate clarified by centrifugation at 17,000 x *g* for 1 hour at 4°C. The His-tagged SUMO-nsp13 was passed through a HisTrap FF column (Cytiva) equilibrated in lysis buffer at 1 ml/minute using a Cytiva Akta FPLC. The affinity resin was washed with 20 column volumes of lysis buffer, and the protein eluted with 10 column volumes of lysis buffer containing 200 mM imidazole. The pooled SUMO-nsp13-containing fractions was dialyzed overnight into two changes of 20 mM imidazole-containing lysis buffer, and the SUMO tag cleaved with Ulp-1 for 4 hours at 4°C. Digestion was confirmed by SDS-PAGE analysis. The His6-Ulp-1 and His6-SUMO proteins were separated from the native nsp13 and nsp13D with a second round of Ni^{2+}-affinity chromatography as before. Helicase-containing flow-thru fractions were pooled, dialyzed overnight against two changes of low salt buffer (50 mM sodium phosphate, pH 6.8, 150 mM NaCl, 4 mM β-mercaptoethanol, 0.5 mM EDTA and 10% glycerol) and passed through a HighTrap SP (Cytiva) cation exchange column. Under these conditions, neither nsp13-helicase prteins adhered to the SP column. The proteins were concentrated with an Amicon Ultra-15 centrifugation filter units to a volume of ~1.5 mls and loaded on to a Sephacyl S200-HR HiPrep 26/60 column (Cytiva) equilibrated with nsp13-helicase Storage Buffer (25 mM HEPES, pH 7.5, 150 mM NaCl, 0.5 mM TCEP and 20% glycerol). The final nsp13-helicase proteins were quantified by UV spectrophotometry at 280 nm using the expected extinction coefficient of 68,785 M^{-1} cm^{-1} and confirmed using the BCA Protein Assay (Pierce). Protein samples were aliquoted, flash frozen, and stored at -80°C.

Recombinant Protein Expression of poliovirus RNA-dependent RNA polymerase.

Poliovirus RdRp was expressed and purified as previously reported (*19*). Briefly, expression was performed at 25°C by auto-induction, cells harvested, lysed by French Press, subjected to PEI precipitation followed by AMS04 precipitation, Ni-NTA chromatography, cleavage by Ulp1, phosphocellulose chromatography, gel filtration and the protein concentrated using Vivaspin concentrators.

Construct fabrication ssRNA template.

The fabrication of the ssRNA template (RNA hairpin) has been described in detail in Ref. (*38*). In brief, the RNA hairpin is made of a 499 bp double-stranded RNA stem terminated by a 20 nt loop that is assembled from three ssRNA annealed together, and two handles, one of 856 bp at the 5′ end and one 822 bp at the 3′ end. The handles include either a 343 nt digoxygenin-labeled ssRNA or a 443 nt biotin-labeled ssRNA to attach to the anti-digoxigenin coated glass surface and the streptavidin-coated magnetic bead (M270), respectively.

Construct fabrication dsRNA template.

The RNA construct used here has been previously described in detail in Ref. (*19*). In brief, a 4 kb long single-stranded splint to which four ssRNAs are annealed: a biotin-labeled strand to attach to the streptavidin-coated magnetic bead (M270), a spacer, ~ 2.9 kb template, and a digoxygenin-labeled strand to attach to the glass surface. The template strand ends in 3′-end with a small hairpin with the sequence ACGCUUUCGCGT followed by 15 U residues to initiate poliovirus RdRp catalyzed RNA synthesis via primer extension.

High-throughput and ultra-stable magnetic tweezers apparatus.

The high-throughput magnetic tweezers used in this study have already been described in detail elsewhere (*24*). Briefly, two vertically aligned permanent magnets (5 mm cubes, SuperMagnete, Switzerland) separated by a 1 mm gap are positioned above a flow cell (see paragraph below) which is mounted on a custom-built inverted microscope. The vertical position and rotation of the magnets are controlled by two linear motors, M-126-PD1 and C-150 (Physik Instrumente PI, GmbH & Co. KG, Karlsruhe, Germany), respectively. The field of view is illuminated through the magnets gap by a collimated LED-light source and is imaged onto a large chip CMOS camera (Dalsa Falcon2 FA-80-12M1H, Stemmer Imaging, Germany) using a 50× oil immersion objective (CFI Plan Achro 50 XH, NA 0.9, Nikon, Germany) and an achromatic doublet tube lens of 200 mm focal length and 50 mm diameter (Qioptic, Germany). To control the temperature, we used a system described in details in Ref. .(*19*). A flexible

resistive foil heater with an integrated 10 MΩ thermistor (HT10K, Thorlabs) is wrapped around the microscope objective and further insulated by several layers 17aptonton tape (KAP22-075, Thorlabs). The heating foil is connected to a PID temperature controller (TC200 PID controller, Thorlabs) to adjust the temperature within ~0.1 °C.

Flow-cell assembly.

The fabrication procedure for flow cells has been described in detail in Ref. (*24*). To summarize, we sandwiched a double layer of Parafilm by two #1 coverslips, the top one having one hole at each end serving as inlet and outlet, the bottom one being coated with a 0.1% m/V nitrocellulose dissolved in amyl acetate solution. The flow cell was mounted into a custom-built holder and rinsed with ~1 ml of 1x phosphate buffered saline (PBS). 3 µm diameter polystyrene reference beads were attached to the bottom coverslip surface by incubating 100 µl of a 1:1000 dilution in PBS (LB30, Sigma Aldrich, stock conc.: 1.828*1011 particles per milliliter) for ~3 minutes. After rinsing the flow cell with 0.5 ml of PBS, 50 µl of anti-digoxigenin (50 µg/ml in PBS) was incubated for 30 minutes in the flow cell. The flow cell was then flushed with 1 ml of 10 mM Tris, 1 mM EDTA pH 8.0, 750 mM NaCl, 2 mM sodium azide to remove excess of anti-digoxigenin followed by rinsing with another 0.5 ml of TE buffer (10 mM Tris, 1 mM EDTA pH 8.0, 150 mM NaCl, 2 mM sodium azide). The surface was then passivated with a solution of bovine serum albumin (BSA, New England Biolabs, 10 mg/ml in PBS and 5% glycerol) for 30 minutes, and rinsed with 0.5 ml of TE buffer.

Single-molecule SARS-CoV-2 RTC activity experiments on dsRNA template.

20 µl of streptavidin coated Dynal Dynabeads M-270 streptavidin coated magnetic beads (ThermoFisher) was mixed with ~0.1 ng of RNA (total volume 40 µl) and incubated for ~5 minutes before rinsing with ~2 ml of TE buffer to remove any unbound RNA and the magnetic beads in excess. RNA tethers were sorted by looking for the characteristic extension of the correct length (~1 µm at 40 pN) due to the stretching of the dsRNA during a force ramp experiment (*38*). The flow cell was subsequently rinsed with 0.5 ml reaction buffer (50 mM HEPES pH 7.9, 10 mM DTT, 2 µM EDTA, 5 mM $MgCl_2$). After starting the data acquisition at the indicated force, 100 µl of reaction buffer containing 0.2 µM nsp12, 1.8 µM nsp7, 1.8 µM nsp8 (1:9:9 stoichiometry), the indicated concentration of nsp13-helicase (WT or mutant if used) and 1 mM NTP were flushed in the flow cell to start the reaction. For the pre-assembled polymerase experiments, all or some of the nsp's were incubated for five minutes in the flow cell, while applying 25 pN force on the tether. The excess RTC proteins were subsequently flushed away with 0.3 ml of reaction buffer (flow cell volume ~ 40 µl), followed by the injection of 100 µl of reaction buffer with desired nsp(s) and 1 mM NTP. The experiments were conducted at a constant force for a duration of 30 to 60 minutes.

The camera frame rate and the temperature were respectively set to 58 Hz and 25°C. A custom written Labview routine controlled the data acquisition and the (x-, y-, z-) positions analysis/tracking of both the magnetic and reference beads in real-time (*39*). Mechanical drift correction was performed by subtracting the reference bead position from the magnetic bead positions and further corrected using an autofocus (i.e. along the z-axis) protocol previously described in Ref. (*17*).

Single-molecule poliovirus RdRp activity experiments on dsRNA template.

20 µl of streptavidin coated Dynal Dynabeads M-270 streptavidin coated magnetic beads (ThermoFisher) was mixed with ~0.1 ng of RNA (total volume 40 µl) and incubated for ~5 minutes before rinsing with ~2 ml of TE buffer to remove any unbound RNA and the magnetic beads in excess. RNA tethers were sorted for functional dsRNA by looking for its characteristic contour length, i.e. ~1 µm. The flow cell was subsequently rinsed with 0.5 ml of reaction buffer (50 mM HEPES pH 7.9, 10 mM DTT, 2 µM EDTA, 5 mM $MgCl_2$). After starting the data acquisition at a suitable force, 100 µl of reaction buffer containing 0.5 µM poliovirus RdRp, indicated concentration of nsp13-helicase and 1 mM NTP were flushed in the flow cell to start the reaction. The experiments were conducted at a constant force for a duration of 30 to 60 minutes.

Single-molecule SARS-CoV-2 RTC activity experiments on ssRNA template.

20 µl of streptavidin-coated Dynal Dynabeads M-270 streptavidin-coated magnetic beads (ThermoFisher Scientific) was mixed with ~0.1 ng of RNA hairpin (total volume 40 µl) and incubated for ~5 min before rinsing with ~2 ml of TE buffer to remove any unbound RNA and the magnetic beads in excess. RNA tethers were sorted for functional hairpins by looking for the characteristic jump in extension of the correct length (~0.6 µm at 30 pN) due to the sudden opening of the hairpin during a force ramp experiment (*38*). The flow cell was subsequently rinsed with 0.5 ml reaction buffer (50 mM HEPES pH 7.9, 10 mM DTT, 2 µM EDTA, and 5 mM MgCl2). After starting the data acquisition at a force (~25 pN) that would keep the hairpin open, 100 µl of reaction buffer containing 0.6 µM of nsp12, 1.8 µM of nsp7 and nsp8 and 20 nM of nsp13-helicase, 500 µM NTP were flushed in the flow cell to start the reaction. The experiments were conducted at a constant force for a duration of 30 to 40 minutes. The camera frame rate was fixed at 58 Hz the temperature set to 25°C. A custom written LabVIEW routine controlled the data acquisition and the (x-, y-, z-) positions analysis/tracking of both the magnetic and reference beads in real time. Mechanical drift correction was performed by subtracting the reference bead position to the magnetic bead position and by applying an autofocus as described in Ref. (*17*).

Data processing.

The activity traces of SARS-CoV-2 RTC or PV RdRp on dsRNA template were first corrected from the mechanical drift by subtracting the reference bead position to the tethers position, then converted from micron to nucleotides using the difference in extension under the same tension of dsRNA and ssRNA, as previously described (*22*). The traces were subsequently low-pass filtered at 0.5 Hz and the dwell-times were extracted using a dwell-time window of 10 nt, as previously described (*19*). Similarly, the data acquired on ssRNA template were filtered at 2 Hz and subsequently converted in nucleotide (*17*). Dwell-times were extracted as for the data on the ssRNA. The dwell-times of all the traces for a given experimental condition were assembled into a single distribution and further analyzed using a maximum likelihood estimation (MLE) fitting routine (*17*) to extract the parameters from the dwell-time fit-function (**Supplementary Materials Section S1**).

Maximum likelihood estimation fitting routine.

The dwell-time distributions were fitted to the experimentally collected dwell-times $\{t_i\}$ by maximizing the log-likelihood function

$$LL = \sum_i \ln P_{N\mathrm{nt}}(t_i) \quad \textbf{(1),}$$

Where $P_{N\mathrm{nt}}$ represents the probability of every dwell-time t_i in the empirical distribution based on the dwell-time fit-function, We calculated the statistical error on the parameters by applying the MLE fitting procedure on 100 bootstraps of the original data set, and reported the standard deviation for each fitting parameter.

To be able to compare fits of models with different number of parameters, we calculated the Bayesian Information Criterion (BIC)

$$\mathrm{BIC} = k\ln(N) - 2\ln(LL). \quad \textbf{(2).}$$

This criterion compares the log-likelihood LL to the number of parameters in the model k and the number of datapoints fitted N to account for the fact that using more parameters can lead to overfitting. The model fit with minimized BIC is considered the best fit with optimal number of parameters for the set of model fits tested (*40*). This criterion compares the log-likelihood LL to the number of parameters in the model k and the number of datapoints fitted N to account for the fact that using more parameters can lead to overfitting. The model fit with minimized BIC is considered the best fit with optimal number of parameters for the set of model fits tested (*40*).

Dwell-time fit-function for nucleotide addition by SARS-CoV-2 core RTC.

The dwell-time distributions of the SARS-CoV-2 RTC in absence of nsp13-helicase were fitted with a fit-function consisting of one gamma distribution with characteristic timescale T_{FNA} fitting the peak at short timescale, two exponential distributions with characteristic timescales T_{SNA} and T_{VSNA} fitting two bumps in the dwell-time distributions and a power law distribution of $\sim t^{-3/2}$ fitting the fat-tail in the dwell-time distributions for longer timescales (*30*)

$$\boldsymbol{P_{Nnt}(t) \approx \frac{f_{FNA}}{T_{FNA}(N-1)!}\left(\frac{tN}{T_{FNA}}\right)^{N-1} e^{-\frac{tN}{T_{FNA}}} + Q(t)\left(\frac{f_{SNA}}{T_{SNA}} e^{-\frac{t-T_{FNA}}{T_{SNA}}} + \frac{f_{VSNA}}{T_{VSNA}} e^{-\frac{t-T_{FNA}}{T_{VSNA}}} + \frac{f_{LLP}\sqrt{1+T_{FNA}}}{2(1+t/1s)^{\frac{3}{2}}}\right)} \qquad \textbf{(3),}$$

with $\sum_j f_j = 1$ for $j \in \{\mathrm{FNA}, \mathrm{SNA}, \mathrm{VSNA}, \mathrm{LLP}\}$ making the distribution $P_{Nnt}(t)$ is correctly normalized. The regularization function $Q(t) = \frac{(t/T_{\mathrm{FNA}})^{N-1}}{1+(t/T_{\mathrm{FNA}})^{N-1}}$ accounts for the fact that the short timescales are dominated by fast nucleotide addition steps. The cut-off is fixed to the FNA peak position, which is the characteristic timescale of the gamma distribution T_{FNA}. Since the exponential distributions start after the peak of the gamma distribution T_{FNA}, the distributions are also normalized starting from T_{FNA}.

For the power law distribution representing a long-lived pause, we have introduced a regularization at 1 s, but the precise timescale does not matter here, as long as it is set within the region dominated by either of the FNA, SNA or VSNA pathways. The power law distribution is cut off with $Q(t)$ and normalized starting from T_{FNA} like the exponential distributions, following the same rationale. We should, however, be careful in interpreting the long-lived pause probability f_{LLP}, since the power law distribution is only an approximate first passage time distribution and should be interpreted as the relative probability for entering the long-lived pause. For a more elaborate discussion, see **Supplementary Information Section S1**.

Considering that we observe a clearly separated peak and two bumps in the dwell-time distributions for the core RTC, we distinguish three characteristic timescales in the dwell-time distribution dominated by fast, slow and very slow nucleotide addition and thus we assume clear separation of timescales for single nucleotide additions $\tau_{\mathrm{FNA}} \ll \tau_{\mathrm{SNA}} \ll \tau_{\mathrm{VSNA}}$. With this assumption, we can derive relations for the characteristic timescales and probabilities in terms of single nucleotide timescales and probabilities as done in (*17*) (**Supplementary Information Section S1**),

$$\begin{aligned}
&\boldsymbol{f_{FNA} = p_{FNA}^{N}}\,, \quad \boldsymbol{T_{FNA} = N\tau_{FNA}}\,,\\
&\boldsymbol{f_{SNA} = (p_{FNA} + p_{SNA})^{N} - p_{FNA}^{N}}\,,\\
&\boldsymbol{f_{VSNA} = (p_{FNA} + p_{SNA} + p_{VSNA})^{N} - (p_{FNA} + p_{SNA})^{N}}\,, \qquad \textbf{(4),}\\
&\boldsymbol{T_{SNA} = \frac{N p_{SNA}(p_{FNA} + p_{SNA})^{N-1}}{(p_{FNA} + p_{SNA})^{N} - p_{FNA}^{N}}\tau_{SNA}}\,,
\end{aligned}$$

$$\boldsymbol{T_{\mathrm{VSNA}} = \frac{N p_{\mathrm{VSNA}} (p_{\mathrm{FNA}}+p_{\mathrm{SNA}}+p_{\mathrm{VSNA}})^{N-1}}{(p_{\mathrm{FNA}}+p_{\mathrm{SNA}}+p_{\mathrm{VSNA}})^{N}-(p_{\mathrm{FNA}}+p_{\mathrm{SNA}})^{N}} \tau_{\mathrm{VSNA}}},$$

Where $p_{\mathrm{FNA}}, p_{\mathrm{SNA}}$ and p_{VSNA} are the probabilities to exit through the FNA, SNA or VSNA pathways for a single nucleotide addition. Furthermore, we added a relative probability to enter the long-lived pause p_{LLP} such that $p_{\mathrm{FNA}} + p_{\mathrm{SNA}} + p_{\mathrm{VSNA}} + p_{\mathrm{LLP}} = 1$ and $\sum_j f_j = 1$ for $j \in \{\mathrm{FNA}, \mathrm{SNA}, \mathrm{VSNA}, \mathrm{LLP}\}$.

Dwell-time fit-function for RNA synthesis on dsRNA by the SARS-CoV-2 RTC in complex with active nsp13-helicase.

The dwell-time distributions for elongation dynamics by the SARS-CoV-2 RTC with active nsp13-helicase were fitted with a dwell-time fit-function consisting of two gamma distributions with characteristic timescales T_{VFNA} and T_{FNA} fitting the two peaks at short timescale, two exponential distributions with timescales T_{SNA} and T_{VSNA} fitting two bumps in the dwell-time distributions and a power law distribution $\sim t^{-3/2}$ fitting the fat-tail in the dwell-time distributions for longer timescales.

The dwell-time fit-function for the dwell-time distributions of RTC elongation dynamics on a dsRNA template in presence of active nsp13-helicase reads

$$P_{N\mathrm{nt}}(t) \approx \frac{f_{\mathrm{VFNA}}}{T_{\mathrm{VFNA}}(N-1)!} N \left(tN/T_{\mathrm{VFNA}}\right)^{N-1} e^{-tN/T_{\mathrm{VFNA}}} + \frac{f_{\mathrm{FNA}}}{T_{\mathrm{FNA}}(N-1)!} N \left(tN/T_{\mathrm{FNA}}\right)^{N-1} e^{-tN/T_{\mathrm{FNA}}} + Q(t)\left(\frac{f_{\mathrm{SNA}}}{T_{\mathrm{SNA}}} e^{-\frac{t-T_{\mathrm{FNA}}}{T_{\mathrm{SNA}}}} + \frac{f_{\mathrm{VSNA}}}{T_{\mathrm{VSNA}}} e^{-\frac{t-T_{\mathrm{FNA}}}{T_{\mathrm{VSNA}}}} + \frac{f_{\mathrm{LLP}}\sqrt{1+T_{\mathrm{FNA}}}}{2(1+t/1s)^{\frac{3}{2}}}\right) \quad \textbf{(5)},$$

with $\sum_j f_j = 1$ for $j \in \{\mathrm{VFNA}, \mathrm{FNA}, \mathrm{SNA}, \mathrm{VSNA}, \mathrm{LLP}\}$ making the distribution $P_{N\mathrm{nt}}(t)$ is correctly normalized and the same regularization function $Q(t) = \frac{(t/T_{\mathrm{FNA}})^{N-1}}{1+(t/T_{\mathrm{FNA}})^{N-1}}$ was used. Since the pauses are sub-dominant under both peaks, the cut-off is fixed to the second gamma peak position, corresponding to the FNA pathway T_{FNA}. Like in the dwell-time fit-function for the core RTC, the two exponential distributions and the power law distribution are cut off by $Q(t)$ and normalised accordingly. The power law distribution also has a regularization at 1 s, since the underlying kinetics are not expected to change in presence of active nsp13-helicase (**Supplementary Information Section S1**). The long-lived pause probability should be interpreted as a relative probability as explained for the fit-function for the core RTC.

Considering two peaks and two bumps could be clearly distinguished in the empirical dwell-time distributions, we obtained four separated characteristic timescales dominated by very fast, fast, slow and

very slow nucleotide addition pathways. Therefore, we could also assume clear separation of single nucleotide timescales $\tau_{\mathrm{VFNA}} \ll \tau_{\mathrm{FNA}} \ll \tau_{\mathrm{SNA}} \ll \tau_{\mathrm{VSNA}}$.

Assembly model for the RTC-nsp13-helicase complexes on a dsRNA template.

We found that the RTC-nsp13 assembly model includes four RTC complexes, i.e. the RTC without nsp13-helicase (core RTC), the RTC with nsp13.1 bound (RTC-nsp13.1), the RTC with the two helicases bound and nsp13.2 not engaged (RTC-nsp13.1,2), the RTC with the two nsp13-helicases bound and nsp13.2 engaged with the non-template RNA (RTC-nsp13.1,2*) (**Fig. 3B**).

We observed very fast nucleotide addition bursts spanning tens to hundreds of nucleotides already for low nsp13-helicase concentration on a dsRNA template (**Fig. 1C**), meaning that the RTC-nsp13.1,2* complex is stable for much longer than the timescale for synthesizing 10 nt RNA (dwell-time window). On top of that, we are mostly interested in unravelling the elongation dynamics at saturating nsp13-helicase concentration compared to the core RTC, so we assume the binding of the two helicases is equilibrated. Under this assumption, the RTC is exclusively in one of the four states during a dwell-time window, so we can write the fractional occupancies p_{cpx} of the complexes $\mathrm{cpx} \in \{\mathrm{c}, 1, 2, 2^*\} = \{\text{core RTC}; \text{RTC} - \text{nsp13.1}; \text{RTC} - \text{nsp13.1,2}; \text{RTC} - \text{nsp13.1,2}^*\}$ in terms of the free-energy barriers between the complexes $\Delta G_{\mathrm{cpx}\to\mathrm{cpx}'}$

$$p_{2^*} = \frac{[\mathrm{nsp13}]^2 e^{-\left(\Delta G_{\mathrm{c}\to 1}+\Delta G_{1\to 2}+\Delta G_{2\to 2^*}\right)}}{Z};$$
$$p_2 = \frac{[\mathrm{nsp13}]^2 e^{-\left(\Delta G_{\mathrm{c}\to 1}+\Delta G_{1\to 2}\right)}}{Z}; \qquad \textbf{(6),}$$
$$p_1 = \frac{[\mathrm{nsp13}] e^{-\Delta G_{\mathrm{c}\to 1}}}{Z}; \quad p_c = \frac{1}{Z};$$

With $Z = [\mathrm{nsp13}]^2 e^{-\left(\Delta G_{c\to 1}+\Delta G_{1\to 2}+\Delta G_{2\to 2^*}\right)} + [\mathrm{nsp13}]^2 e^{-\left(\Delta G_{c\to 1}+\Delta G_{1\to 2}\right)} + [\mathrm{nsp13}] e^{-\Delta G_{c\to 1}} + 1$. The free-energy barriers between the complexes $\Delta G_{\mathrm{cpx}\to\mathrm{cpx}'}$ are in terms of $k_{\mathrm{B}}T$. Here we used that the fraction of product of every single equilibrium reaction is given by a Boltzmann factor dependent on the nsp13-helicase concentration and the free-energy barrier (*41*). The RTC-nsp13.1,2* fractional occupancy fitted well to the VFNA probability versus nsp13-helicase concentration (**Fig. S4**).

Furthermore, the association constants for nsp13.1 and nsp13.2 to the RTC could be obtained from the free-energy barriers in the assembly model as

$$K_{\mathrm{a,nsp13.1}} = e^{-\Delta G_{\mathrm{c}\to 1}}; \qquad K_{\mathrm{a,nsp13.2}} = e^{-\Delta G_{1\to 2}} \qquad \textbf{(7),}$$

with nM^{-1} as unit.

Integrating the assembly of the RTC-nsp13-helicase complexes with the elongation dynamics on a dsRNA template in presence of active nsp13-helicase.

We then built the RTC Assembly-Elongation dynamics model connecting the RTC assembly model with the elongation dynamics (dwell-time fit-function) for a mix of core RTC's and RTC-nsp13 complexes with a constant tension on the non-template RNA strand.

Since we can assume that the RTC resides exclusively in one of the RTC-nsp13 states within one dwell-time window, as stated above, the first passage time distribution for elongation dynamics by a mix of core RTC and RTC-nsp13 complexes was obtained by summing the first passage time distributions $P_{10\mathrm{nt}}(t|\mathrm{cpx})$ for the different RTC complexes $\mathrm{cpx} \in \{\mathrm{c}, 1, 2, 2^*\} = \{\mathrm{core\ RTC};\ \mathrm{RTC-nsp13.1};\ \mathrm{RTC-nsp13.1{,}2};\ \mathrm{RTC-nsp13.1{,}2^*}\}$ with the fractional occupancies for each RTC complex p_{cpx} as pre-factor

$$P_{N\mathrm{nt,RTC-nsp13}}(t) = \sum_{\mathrm{cpx}} p_{\mathrm{cpx}} P_{10\mathrm{nt}}(t|\mathrm{cpx}) \quad \textbf{(8),}$$

are the first passage time distributions conditioned that the RTC resides in complex cpx for the 10 nt of interest. As previously described, we approximate the first passage time distribution for each RTC complex by the dwell-time fit-function (**Eq. 3**). Considering $P_{10\mathrm{nt}}(t|\mathrm{cpx})$ is also a summation of terms with separated characteristic timescales T_{j} for each pathway $\mathrm{NA} \in \{\mathrm{VFNA, FNA, SNA, VSNA}\}$ and that the timescales stay within one order of magnitude from the core RTC to saturating nsp13-helicase condition (**Fig. 3C**), we obtained the average characteristic timescale of each NA pathway T_{NA} and the combined probability f_{NA} in the RTC-nsp13 mixture, referred to as the effective parameters (**Supplementary Information Section S2**)

$$\begin{aligned}
f_{\mathrm{VFNA}} &= p_{2^*}\,, \\
T_{\mathrm{VFNA}} &= N\tau_{\mathrm{VFNA}}\,, \\
f_{\mathrm{FNA}} &= \sum_{\mathrm{cpx}} p_{\mathrm{cpx}} \left(p_{\mathrm{FNA}}^{\mathrm{cpx}}\right)^N, \\
T_{\mathrm{FNA}} &= \frac{\sum_{\mathrm{cpx}} p_{\mathrm{cpx}} \left(p_{\mathrm{FNA}}^{\mathrm{cpx}}\right)^N N\tau_{\mathrm{FNA}}^{\mathrm{cpx}}}{\sum_{\mathrm{cpx}} p_{\mathrm{cpx}} \left(p_{\mathrm{FNA}}^{\mathrm{cpx}}\right)^N}\,, \\
f_{\mathrm{SNA}} &= \sum_{\mathrm{cpx}} p_{\mathrm{cpx}} \left[\left(p_{\mathrm{FNA}}^{\mathrm{cpx}} + p_{\mathrm{SNA}}^{\mathrm{cpx}}\right)^N - \left(p_{\mathrm{FNA}}^{\mathrm{cpx}}\right)^N\right], \\
T_{\mathrm{SNA}} &= \frac{\sum_{\mathrm{cpx}} p_{\mathrm{cpx}} p_{\mathrm{SNA}}^{\mathrm{cpx}} \left(p_{\mathrm{FNA}}^{\mathrm{cpx}} + p_{\mathrm{SNA}}^{\mathrm{cpx}}\right)^{N-1} N\tau_{\mathrm{SNA}}^{\mathrm{cpx}}}{\sum_{\mathrm{cpx}} p_{\mathrm{cpx}} \left[\left(p_{\mathrm{FNA}}^{\mathrm{cpx}} + p_{\mathrm{SNA}}^{\mathrm{cpx}}\right)^N - \left(p_{\mathrm{FNA}}^{\mathrm{cpx}}\right)^N\right]}, \\
f_{\mathrm{VSNA}} &= \sum_{\mathrm{cpx}} p_{\mathrm{cpx}} \left[\left(p_{\mathrm{FNA}}^{\mathrm{cpx}} + p_{\mathrm{SNA}}^{\mathrm{cpx}} + p_{\mathrm{VSNA}}^{\mathrm{cpx}}\right)^N - \left(p_{\mathrm{FNA}}^{\mathrm{cpx}} + p_{\mathrm{SNA}}^{\mathrm{cpx}}\right)^N\right],
\end{aligned} \quad \textbf{(9),}$$

$$T_{\mathrm{VSNA}} = \frac{\sum_{\mathrm{cpx}} p_{\mathrm{cpx}} p_{\mathrm{VSNA}}^{\mathrm{cpx}} \left(p_{\mathrm{FNA}}^{\mathrm{cpx}} + p_{\mathrm{SNA}}^{\mathrm{cpx}} + p_{\mathrm{VSNA}}^{\mathrm{cpx}}\right)^{N-1} N \tau_{\mathrm{VSNA}}^{\mathrm{cpx}}}{\sum_{\mathrm{cpx}} p_{\mathrm{cpx}} \left[\left(p_{\mathrm{FNA}}^{\mathrm{cpx}} + p_{\mathrm{SNA}}^{\mathrm{cpx}} + p_{\mathrm{VSNA}}^{\mathrm{cpx}}\right)^{N} - \left(p_{\mathrm{FNA}}^{\mathrm{cpx}} + p_{\mathrm{SNA}}^{\mathrm{cpx}}\right)^{N}\right]}$$

For RTC complexes $\mathrm{cpx} \in \{\mathrm{c}, 1, 2\} = \{\mathrm{core\ RTC};\ \mathrm{RTC-nsp13.1};\ \mathrm{RTC-nsp13.1,2}\}$, considering that the FNA, SNA, VSNA pathway are not entered by the RTC-nsp13.1,2* complex. For a fit to the dwell-time distributions, the expressions for the average characteristic timescales and combined probabilities **Eq. 9** were substituted into the dwell-time fit function **Eq. 5**. Furthermore, we added a relative probability to enter the long-lived pause for each RTC complex $p_{\mathrm{LLP}}^{\mathrm{cpx}}$ such that $p_{\mathrm{FNA}}^{\mathrm{cpx}} + p_{\mathrm{SNA}}^{\mathrm{cpx}} + p_{\mathrm{VSNA}}^{\mathrm{cpx}} + p_{\mathrm{LLP}}^{\mathrm{cpx}} = 1$ and thus $\sum_j f_j = 1$ for $j \in \{\mathrm{FNA}, \mathrm{SNA}, \mathrm{VSNA}, \mathrm{LLP}\}$. The VFNA and VSNA characteristic timescales were fixed to $T_{\mathrm{VFNA}} = 0.2$ s and $T_{\mathrm{VSNA}} = 4.8$ s respectively, so the corresponding single nucleotide timescales $\tau_{\mathrm{VFNA}}, \tau_{\mathrm{VSNA}}^{\mathrm{c}}, \tau_{\mathrm{VSNA}}^{2}$ were not fitted, but could be directly retrieved from **Eq. 9**.

As explained in the **Results** section, we kept all single nucleotide parameters in the RTC-nsp13.1 complex the same as for the core RTC, while the parameters were free variables for the RTC-nsp13.1,2 complex. The free parameters in the RTC assembly - Elongation dynamics model are the single nucleotide probabilities $p_{\mathrm{FNA}}^{\mathrm{c}}$, $p_{\mathrm{SNA}}^{\mathrm{c}}$, $p_{\mathrm{VSNA}}^{\mathrm{c}}$, p_{FNA}^{2}, p_{SNA}^{2}, p_{VSNA}^{2} and the single nucleotide timescales $\tau_{\mathrm{FNA}}^{\mathrm{c}}$, $\tau_{\mathrm{SNA}}^{\mathrm{c}}, \tau_{\mathrm{FNA}}^{2}$, τ_{SNA}^{2} for the core RTC (c) and RTC-nsp13.1,2 (2) complex and the free-energy barriers in the RTC assembly model $\Delta G_{\mathrm{c}\to 1}$, $\Delta G_{1\to 2}$, $\Delta G_{2\to 2^*}$.

To perform a global fit on the empirical dwell-time distributions versus nsp13-helicase concentration, we obtained the average characteristic timescales and the combined probability for each pathway at every nsp13-helicase concentration measured from the RTC Assembly - Elongation dynamics model (**Eq. 9** with **Eq. 6** substituted) and substituted these parameters into the dwell-time fit-function **Eq. 5** with VFNA and VSNA characteristic timescales fixed to $T_{\mathrm{VFNA}} = 0.2$ s and $T_{\mathrm{VSNA}} = 4.8$ s respectively. In this way, we obtained a probability density function for each condition measured, which could be successfully fitted to the dwell-time distributions (**Fig. 3A**) using the Maximum likelihood fitting routine (see **Materials and Methods**).

Building the mechanochemical model underlying the RNA tension dependency of the RTC elongation dynamics in absence or presence of nsp13-helicase.

The force dependence of a kinetic rate can be captured by the Arrhenius equation

$$\boldsymbol{k_{\mathrm{X}}(F) = k_{\mathrm{X},0} e^{\delta_X F / k_{\mathrm{B}} T}} \qquad \textbf{(10),}$$

Where δ_X is the distance to the transition state and $k_{\mathrm{X},0}$ is the rate at zero force. Important to mention is that this relation applies both for an assisting force F or opposing force $-F$. In the case of a dsRNA template,

the force (tension) is applied on the non-template RNA strand, which acts as an assisting force on elongation by the RTC.

In our mechanochemical model (**Fig. 4G**), derived based on the trends observed in the characteristic timescales and probabilities versus RNA tension with or without saturating nsp13-helicase concentration (**Results, Fig. 4C-F, Supplementary Information**), we only have a force (RNA tension) dependence on the backward translocation rates in the FNA and SNA pathway for the core RTC, RTC-nsp13.1 and RTC-nsp13.1,2 complex. Translocation acts over the distance from the conversion of one base pair dsRNA to ssRNA $a = \delta x_{\mathrm{ss}} - \delta x_{\mathrm{ds}} \approx 0.2$ nm (Dulin et al. 2015). Therefore, the opposing RNA tension (F) dependency on the backward translocation rate can be described as the Arrhenius law with distance a

$$k_{\mathrm{pre}}^{\mathrm{NA,cpx}}(F) = k_{\mathrm{pre}}^{\mathrm{NA,cpx}}(0)e^{-aF/k_{\mathrm{B}}T}, \qquad \mathrm{NA} \in \{\mathrm{FNA}, \mathrm{SNA}\}, \qquad \mathrm{cpx} \in \{\mathrm{c}, 1, 2\} \qquad \textbf{(11),}$$

To obtain the expressions for the timescale and probability for a single nucleotide addition in pathway $\mathrm{NA} \in \{\mathrm{FNA}, \mathrm{SNA}\}$ (the pathways that show an RNA tension dependency in the characteristic timescale) in each RTC complex $\mathrm{cpx} \in \{\mathrm{c}, 1{,}2\} = \{\mathrm{core\ RTC};\ \mathrm{RTC-nsp13.1};\ \mathrm{RTC-nsp13.1{,}2}\}$, we constructed the first passage time distribution for completing the irreversible step in pathway NA, considering that translocation is not equilibrated, by summing over all possible paths with forward and backward translocation (with rates $k_{\mathrm{post}}^{\mathrm{NA,cpx}}$ and $k_{\mathrm{pre}}^{\mathrm{NA,cpx}}(F)$ respectively) followed by NTP binding and catalysis with rate $k_{\mathrm{irr}}^{\mathrm{NA,cpx}}$ (**Fig 4G**). In Laplace space the first passage time distribution is written as

$$\Psi_{\mathrm{irr}}^{\mathrm{NA,cpx}}(s) = \frac{k_{\mathrm{irr}}^{\mathrm{NA}} k_{\mathrm{post}}^{\mathrm{NA}}}{\left(s + k_{\mathrm{post}}^{\mathrm{NA}} + k_{\mathrm{out}}^{\mathrm{NA}}\right)\left(s + k_{\mathrm{pre}}^{\mathrm{NA,cpx}}(F) + k_{\mathrm{irr}}^{\mathrm{NA}}\right) - k_{\mathrm{post}}^{\mathrm{NA}} k_{\mathrm{pre}}^{\mathrm{NA,cpx}}(F)} \qquad \textbf{(12),}$$

With $k_{\mathrm{out}}^{\mathrm{FNA}} = k_{\mathrm{in}}^{\mathrm{SNA}} + k_{\mathrm{in}}^{\mathrm{LLP}}$; $k_{\mathrm{out}}^{\mathrm{SNA}} = k_{\mathrm{in}}^{\mathrm{VSNA}} + k_{\mathrm{in}}^{\mathrm{LLP}}$, where $k_{\mathrm{in}}^{\mathrm{j}}$ are the rates to enter pathway $j \in \{\mathrm{SNA}, \mathrm{VSNA}, \mathrm{LLP}\}$, which are the same for the core RTC and the nsp13-bound RTC complexes $\mathrm{cpx} \in \{\mathrm{c}, 1, 2\} = \{\mathrm{core\ RTC};\ \mathrm{RTC-nsp13.1};\ \mathrm{RTC-nsp13.1{,}2}\}$.

We obtained the probability and timescales of completing the irreversible step in pathway $\mathrm{NA} \in \{\mathrm{FNA}, \mathrm{SNA}\}$ as the zeroth and first moment of the distribution $p_{\mathrm{irr}}^{\mathrm{NA,cpx}}(t)$, the inverse Laplace transform of $\Psi_{\mathrm{irr}}^{\mathrm{NA,cpx}}(s)$, respectively

$$p_{\mathrm{irr}}^{\mathrm{NA,cpx}} = \Psi_{\mathrm{irr}}^{\mathrm{NA,cpx}}(0) = \frac{k_{\mathrm{irr}}^{\mathrm{NA}} k_{\mathrm{post}}^{\mathrm{NA}}}{\left(k_{\mathrm{post}}^{\mathrm{NA}} + k_{\mathrm{out}}^{\mathrm{NA}}\right)\left(k_{\mathrm{pre}}^{\mathrm{NA,cpx}}(F) + k_{\mathrm{irr}}^{\mathrm{NA}}\right) - k_{\mathrm{post}}^{\mathrm{NA}} k_{\mathrm{pre}}^{\mathrm{NA,cpx}}(F)};$$

$$\tau_{\mathrm{irr}}^{\mathrm{NA,cpx}} = -\partial_s \ln \Psi_{\mathrm{irr}}^{\mathrm{NA,cpx}}(0) = \frac{k_{\mathrm{post}}^{\mathrm{NA}} + k_{\mathrm{out}}^{\mathrm{NA}} + k_{\mathrm{pre}}^{\mathrm{NA,cpx}}(F) + k_{\mathrm{irr}}^{\mathrm{NA}}}{\left(k_{\mathrm{post}}^{\mathrm{NA}} + k_{\mathrm{out}}^{\mathrm{NA}}\right)\left(k_{\mathrm{pre}}^{\mathrm{NA,cpx}}(F) + k_{\mathrm{irr}}^{\mathrm{NA}}\right) - k_{\mathrm{post}}^{\mathrm{NA}} k_{\mathrm{pre}}^{\mathrm{NA,cpx}}(F)}; \qquad \textbf{(13),}$$

With $k_{\mathrm{out}}^{\mathrm{FNA}} = k_{\mathrm{in}}^{\mathrm{SNA}} + k_{\mathrm{in}}^{\mathrm{LLP}}$; $k_{\mathrm{out}}^{\mathrm{SNA}} = k_{\mathrm{in}}^{\mathrm{VSNA}} + k_{\mathrm{in}}^{\mathrm{LLP}}$.

Considering that the slowest pathway entered is dominating the timescale of the single nucleotide addition, we have $\tau_{\mathrm{NA}}^{\mathrm{cpx}} = \tau_{\mathrm{irr}}^{\mathrm{NA,cpx}}$. To obtain the single nucleotide probability for each pathway $\mathrm{NA} \in \{\mathrm{FNA}, \mathrm{SNA}, \mathrm{VSNA}\}$ and the RTC complexes $\mathrm{cpx} \in \{1, 2, 2^*\}$, we have to consider that we start each NA cycle from the FNA pre-translocated state, from which the SNA pre-translocated state can be entered and from there the VSNA pre-translocated state (**Fig. 4G**). Furthermore, the long-lived pause can be entered from each NA pre-translocated state. Therefore, the single nucleotide probabilities for exiting through the pathways are obtained as

$$
\begin{aligned}
&p_{\mathrm{FNA}}^{\mathrm{cpx}}(F) = p_{\mathrm{irr}}^{\mathrm{FNA,cpx}}(F);\\
&p_{\mathrm{SNA}}^{\mathrm{cpx}}(F) = \left(1 - p_{\mathrm{irr}}^{\mathrm{FNA,cpx}}(F)\right)\frac{k_{\mathrm{in}}^{\mathrm{SNA}}}{k_{\mathrm{out}}^{\mathrm{FNA}}}p_{\mathrm{irr}}^{\mathrm{SNA,cpx}}(F);\\
&p_{\mathrm{VSNA}}^{\mathrm{cpx}}(F) = \left(1 - p_{\mathrm{irr}}^{\mathrm{FNA,cpx}}(F)\right)\frac{k_{\mathrm{in}}^{\mathrm{SNA}}}{k_{\mathrm{out}}^{\mathrm{FNA}}}\left(1 - p_{\mathrm{irr}}^{\mathrm{SNA,cpx}}(F)\right)\frac{k_{\mathrm{in}}^{\mathrm{VSNA}}}{k_{\mathrm{out}}^{\mathrm{SNA}}}p_{\mathrm{irr}}^{\mathrm{VSNA,cpx}};\\
&p_{\mathrm{LLP}}^{\mathrm{cpx}}(F) = 1 - p_{\mathrm{FNA}}^{\mathrm{cpx}}(F) - p_{\mathrm{SNA}}^{\mathrm{cpx}}(F) - p_{\mathrm{VSNA}}^{\mathrm{cpx}}(F)
\end{aligned}
\qquad \textbf{(14),}
$$

The allosteric effect of nsp13.2 binding to the RTC, resulting in decreased FNA and SNA single nucleotide timescale accompanied by a decreased SNA and VSNA probability for the RTC-nsp13.1,2 complex (**Table S2**), can be modelled as an increase in the free-energy barrier ΔG_{NA} for backward translocation rate in each NA pathway

$$k_{\mathrm{pre}}^{\mathrm{NA,2}}(F) = k_{\mathrm{pre}}^{\mathrm{NA,c}}(F)e^{\Delta G_{\mathrm{NA}}}, \qquad \mathrm{NA} \in \{\mathrm{FNA}, \mathrm{SNA}\} \qquad \textbf{(15).}$$

Since the VSNA characteristic timescale was fixed in the fits, the underlying mechanochemistry cannot be extracted from it, so we directly fit $p_{\mathrm{irr}}^{\mathrm{VSNA,cpx}}$ for $\mathrm{cpx} \in \{1, 2\}$.

All parameters in the mechanochemical model for the RTC-nsp13.1 complex were the same as for the core RTC. As a result, the free parameters in the mechanochemical model were $k_{\mathrm{in}}^{\mathrm{SNA}}, k_{\mathrm{in}}^{\mathrm{VSNA}}, k_{\mathrm{in}}^{\mathrm{LLP}}, k_{\mathrm{post}}^{\mathrm{FNA}}, k_{\mathrm{post}}^{\mathrm{SNA}}, k_{\mathrm{pre}}^{\mathrm{FNA.c}}(0), k_{\mathrm{pre}}^{\mathrm{FNA.2}}(0), k_{\mathrm{pre}}^{\mathrm{SNA.c}}(0), k_{\mathrm{pre}}^{\mathrm{SNA.2}}(0), k_{\mathrm{irr}}^{\mathrm{FNA}}, k_{\mathrm{irr}}^{\mathrm{SNA}}, p_{\mathrm{irr}}^{\mathrm{VSNA.c}}, p_{\mathrm{irr}}^{\mathrm{VSNA.2}}$ giving the single nucleotide probabilities and timescales. The substitution into the RTC Assembly - Elongation dynamics model added the free-energy barriers between the states in the RTC-nsp13 assembly model $\Delta G_{\mathrm{c}\to 1}$, $\Delta G_{1\to 2}$, $\Delta G_{2\to 2^*}$.

A global fit of the mechanochemical model was successfully performed on the dwell-time distributions of the nsp13-helicase concentration dependency dataset at 20 pN RNA tension and RNA tension dependency datasets without nsp13-helicase and at saturating nsp13-helicase concentration (20 nM) (**Fig. 3ACD & 4C-F**, **Fig. S14**). To be able to fit the mechanochemical model to the dwell-time distributions for all conditions, we substituted the expressions for the single nucleotide timescales and probabilities versus RNA tension (**Eq. 13** and **Eq. 14** substituted with **Eq. 11**) in the RTC Assembly - Elongation

dynamics model (**Eq. 9** with **Eq. 6** substituted) to obtain the effective parameters. Sequentially, these parameters were substituted into the dwell-time fit-function **Eq. 5** and we fixed the VFNA and VSNA characteristic timescales to 0.2 s and 4.8 s respectively. In this way, we obtained a pdf curve for each condition measured, which were successfully fitted to the empirical dwell-time distributions (**Fig. S14**). A more thorough explanation of the argumentation for and derivation of the mechanochemical model can be found in **Supplementary information Section S3**.

Performing fits, bootstrapping and fit selection.

For each model fit on the empirical dwell-time distributions, we performed multiple fits to check the fitting robustness for the boundaries set and selected the best fit. Then we performed 100 bootstrap fits for each model, on resampled dwell-time distributions, from which we obtained the mean value and standard deviation on each parameter in the fitted model. Next to the check whether the fit parameters are within the set boundary values, we checked during the MLE fitting procedure for the dwell-time fit-function that none of the probabilities had a negative value and the sum of the probabilities was 1 for every condition. During the MLE fitting procedure of the RTC Assembly – Elongation dynamics model, we also checked whether the conditions $\tau_{\mathrm{VFNA}} \ll \tau_{\mathrm{FNA}.i} \ll \tau_{\mathrm{SNA}.i} \ll \tau_{\mathrm{VSNA}.i}$ applies for the single nucleotide timescales for each RTC complex $\mathrm{cpx} \in \{c, 1,\ 2\} = \{\mathrm{core\ RTC};\ \mathrm{RTC-nsp13.1};\ \mathrm{RTC-nsp13.1,2}\}$ to make sure the separation of timescales applies (**Table S2**). During the MLE fitting procedure of the mechanochemical model, we set the condition that the forward translocation rate should be equal or larger in the FNA pathway than in the SNA pathway ($k_{\mathrm{post,FNA}}$ and $k_{\mathrm{post,SNA}}$ respectively) (**Table S3**).

Additionally, we set certain parameters constant during the fitting, with the goal to minimize the number of free parameters in the model without marginalizing the goodness-of-fit using the Bayesian Information Criterion (BIC) as a guide. Following this argumentation, we performed fits of the dwell-time fit-function with the characteristic timescale of the VFNA and VSNA pathway fixed to 0.2 s and 4.8 s respectively for the various conditions measured (**Fig. S2, Supplementary Information Section S1**). For the fits of the RTC Assembly – Elongation dynamics model we also checked whether some of the single nucleotide parameters could be fixed for a similar goodness-of-fit, for a detailed explanation refer to (**Supplementary Information Section S2**).

References

1. K. C. Lehmann, E. J. Snijder, C. C. Posthuma, A. E. Gorbalenya, What we know but do not understand about nidovirus helicases. *Virus Res* **202**, 12-32 (2015).
2. A. E. Gorbalenya, E. V. Koonin, Viral proteins containing the purine NTP-binding sequence pattern. *Nucleic acids research* **17**, 8413-8440 (1989).
3. J. C. Marecki, B. Belachew, J. Gao, K. D. Raney, RNA helicases required for viral propagation in humans. *Enzymes* **50**, 335-367 (2021).
4. J. Chen *et al.*, Structural Basis for Helicase-Polymerase Coupling in the SARS-CoV-2 Replication-Transcription Complex. *Cell* **182**, 1560-1573 e1513 (2020).
5. T. Osawa, M. Aoki, H. Ehara, S. I. Sekine, Structures of dengue virus RNA replicase complexes. *Mol Cell* **83**, 2781-2791 e2784 (2023).
6. Y. B. Tan *et al.*, Molecular architecture of the Chikungunya virus replication complex. *Sci Adv* **8**, eadd2536 (2022).
7. B. Malone, N. Urakova, E. J. Snijder, E. A. Campbell, Structures and functions of coronavirus replication-transcription complexes and their relevance for SARS-CoV-2 drug design. *Nature reviews. Molecular cell biology* **23**, 21-39 (2022).
8. H. S. Hillen *et al.*, Structure of replicating SARS-CoV-2 polymerase. *Nature*, (2020).
9. R. N. Kirchdoerfer, A. B. Ward, Structure of the SARS-CoV nsp12 polymerase bound to nsp7 and nsp8 co-factors. *Nature communications* **10**, 2342 (2019).
10. H. S. Hillen, Structure and function of SARS-CoV-2 polymerase. *Curr Opin Virol* **48**, 82-90 (2021).
11. L. Yan *et al.*, Architecture of a SARS-CoV-2 mini replication and transcription complex. *Nature communications* **11**, 5874 (2020).
12. S. L. Grimes, M. R. Denison, The Coronavirus helicase in replication. *Virus Res* **346**, 199401 (2024).
13. J. A. Newman *et al.*, Structure, mechanism and crystallographic fragment screening of the SARS-CoV-2 NSP13 helicase. *Nature communications* **12**, 4848 (2021).
14. K. J. Mickolajczyk *et al.*, Force-Dependent Stimulation of RNA Unwinding by SARS-CoV-2 nsp13 Helicase. *Biophysical journal*, (2020).
15. S. K. Marx *et al.*, Observing inhibition of the SARS-CoV-2 helicase at single-nucleotide resolution. *Nucleic acids research* **51**, 9266-9278 (2023).
16. J. Chen *et al.*, Ensemble cryo-EM reveals conformational states of the nsp13 helicase in the SARS-CoV-2 helicase replication-transcription complex. *Nature structural & molecular biology* **29**, 250-260 (2022).
17. S. C. Bera *et al.*, The nucleotide addition cycle of the SARS-CoV-2 polymerase. *Cell Rep* **36**, 109650 (2021).
18. I. Manfredonia *et al.*, Genome-wide mapping of SARS-CoV-2 RNA structures identifies therapeutically-relevant elements. *Nucleic acids research*, (2020).
19. M. Seifert *et al.*, Temperature controlled high-throughput magnetic tweezers show striking difference in activation energies of replicating viral RNA-dependent RNA polymerases. *Nucleic acids research* **48**, 5591-5602 (2020).
20. D. Dulin *et al.*, Signatures of Nucleotide Analog Incorporation by an RNA-Dependent RNA Polymerase Revealed Using High-Throughput Magnetic Tweezers. *Cell Rep* **21**, 1063-1076 (2017).
21. D. Dulin, in *Single Molecule Analysis : Methods and Protocols,* I. Heller, D. Dulin, E. J. G. Peterman, Eds. (Springer US, New York, NY, 2024), pp. 375-401.
22. D. Dulin *et al.*, Elongation-Competent Pauses Govern the Fidelity of a Viral RNA-Dependent RNA Polymerase. *Cell Rep* **10**, 983-992 (2015).
23. E. Ostrofet, F. S. Papini, D. Dulin, Correction-free force calibration for magnetic tweezers experiments. *Sci Rep* **8**, 15920 (2018).

24. S. Quack, D. Dulin, in *Single Molecule Analysis : Methods and Protocols,* I. Heller, D. Dulin, E. J. G. Peterman, Eds. (Springer US, New York, NY, 2024), pp. 403-420.
25. Y. Gao *et al.*, Structure of the RNA-dependent RNA polymerase from COVID-19 virus. *Science (New York, N.Y* **368**, 779-782 (2020).
26. S. K. Marx *et al.*, Observing inhibition of the SARS-CoV-2 helicase at single-nucleotide resolution. *Nucleic Acids Res* **51**, 9266-9278 (2023).
27. M. Seifert *et al.*, Inhibition of SARS-CoV-2 polymerase by nucleotide analogs from a single-molecule perspective. *eLife* **10**, (2021).
28. B. Malone *et al.*, Structural basis for backtracking by the SARS-CoV-2 replication-transcription complex. *Proceedings of the National Academy of Sciences of the United States of America* **118**, (2021).
29. D. Dulin, B. A. Berghuis, M. Depken, N. H. Dekker, Untangling reaction pathways through modern approaches to high-throughput single-molecule force-spectroscopy experiments. *Curr Opin Struct Biol* **34**, 116-122 (2015).
30. M. Depken, E. A. Galburt, S. W. Grill, The origin of short transcriptional pauses. *Biophysical journal* **96**, 2189-2193 (2009).
31. I. Grossman-Haham, G. Rosenblum, T. Namani, H. Hofmann, Slow domain reconfiguration causes power-law kinetics in a two-state enzyme. *Proceedings of the National Academy of Sciences of the United States of America* **115**, 513-518 (2018).
32. M. L. Agostini *et al.*, Coronavirus Susceptibility to the Antiviral Remdesivir (GS-5734) Is Mediated by the Viral Polymerase and the Proofreading Exoribonuclease. *Mbio* **9**, (2018).
33. A. Jayk Bernal *et al.*, Molnupiravir for Oral Treatment of Covid-19 in Nonhospitalized Patients. *N Engl J Med* **386**, 509-520 (2022).
34. C. J. Gordon *et al.*, Remdesivir is a direct-acting antiviral that inhibits RNA-dependent RNA polymerase from severe acute respiratory syndrome coronavirus 2 with high potency. *The Journal of biological chemistry* **295**, 6785-6797 (2020).
35. J. P. K. Bravo, T. L. Dangerfield, D. W. Taylor, K. A. Johnson, Remdesivir is a delayed translocation inhibitor of SARS-CoV-2 replication. *Molecular Cell* **81**, 1548-+ (2021).
36. G. Kokic *et al.*, Mechanism of SARS-CoV-2 polymerase stalling by remdesivir. *Nature communications* **12**, 279 (2021).
37. B. Sama *et al.*, The effects of Remdesivir's functional groups on its antiviral potency and resistance against the SARS-CoV-2 polymerase. *Antiviral research* **232**, 106034 (2024).
38. F. S. Papini, M. Seifert, D. Dulin, High-yield fabrication of DNA and RNA constructs for single molecule force and torque spectroscopy experiments. *Nucleic acids research* **47**, e144 (2019).
39. J. P. Cnossen, D. Dulin, N. H. Dekker, An optimized software framework for real-time, high-throughput tracking of spherical beads. *The Review of scientific instruments* **85**, 103712 (2014).
40. S. Konishi, G. Kitagawa, *Information criteria and statistical modeling*. Springer series in statistics (Springer, New York, 2008), pp. xii, 273 p.
41. R. Phillips, J. Kondev, J. Theriot, *Physical biology of the cell*. (Garland Science, New York, 2009), pp. xxiv, 807 p.

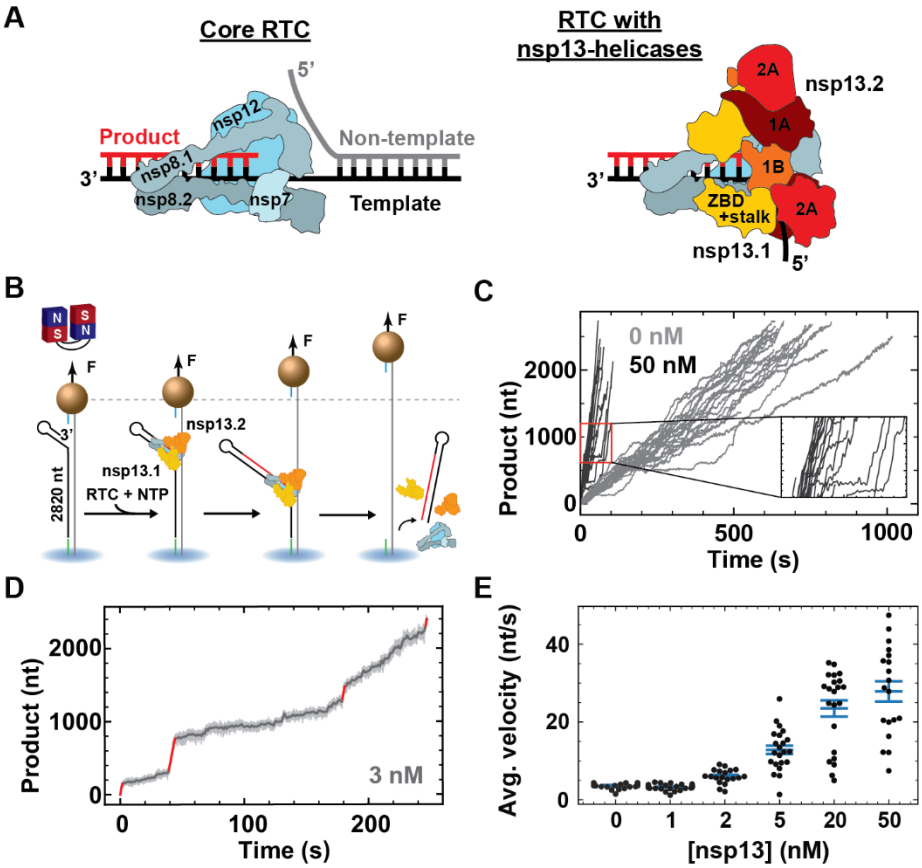

Figure 1: The SARS-CoV-2 nsp13-helicase enables fast RTC elongation on dsRNA. (A) Core RTC alone (left) and in association with two nsp13-helicases (right). Core RTC subunits (left) and nsp13-helicase domains (right) are indicated. **(B)** Schematic of the magnetic tweezers assay to monitor RTC elongation on dsRNA with nsp13-helicase. **(C)** Elongation traces obtained without (grey) or with (black) 50 nM nsp13-helicase at 20 pN RNA tension. (inset) Zoom in on traces at saturating nsp13-helicase concentration still show some slow dynamics alternating the long bursts of very fast nucleotide addition. **(D)** Elongation trace obtained at 3 nM nsp13-helicase. The bursts of very fast nucleotide addition are highlighted (red). The raw and filtered trace are shown (light grey and dark grey). **(E)** Average elongation velocity (nt/s) versus nsp13-helicase concentration from single traces that show elongation for at least 1000 nt (dots). Mean and errorbars of one standard deviation are indicated (blue bars).

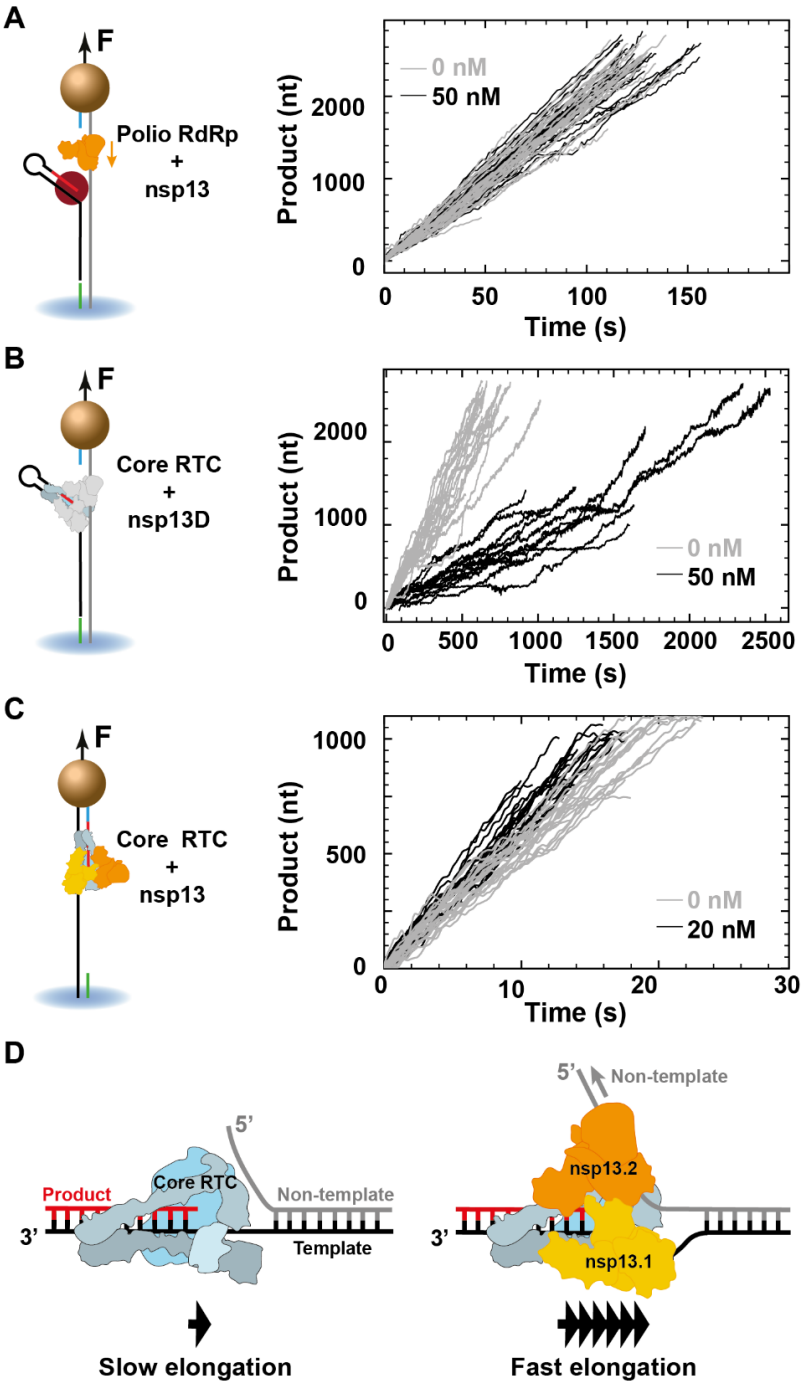

Figure 2: Nsp13-helicase specifically associates with the SARS-CoV-2 core RTC and nsp13.2 assists its elongation by translocating on the non-template RNA strand. (A, B, C) On the left, schematics describing the measurements performed with nsp13-helicase using either (A) poliovirus RdRp or (B, C) SARS-CoV-2 core RTC elongating on either a dsRNA (A, B) or ssRNA (C) template, with either wild-type nsp13-helicase (A, C) or ATPase dead K288A nsp13-helicase mutant (B). The corresponding elongation activity traces are shown on the right, i.e. without (grey) or with (black) nsp13-helicase at the indicated concentration. **(D)** Model resuming the observations. The core RTC elongates slowly against duplex RNA, and very fast elongation is recovered when the RTC specifically associates with nsp13-helicases (A).

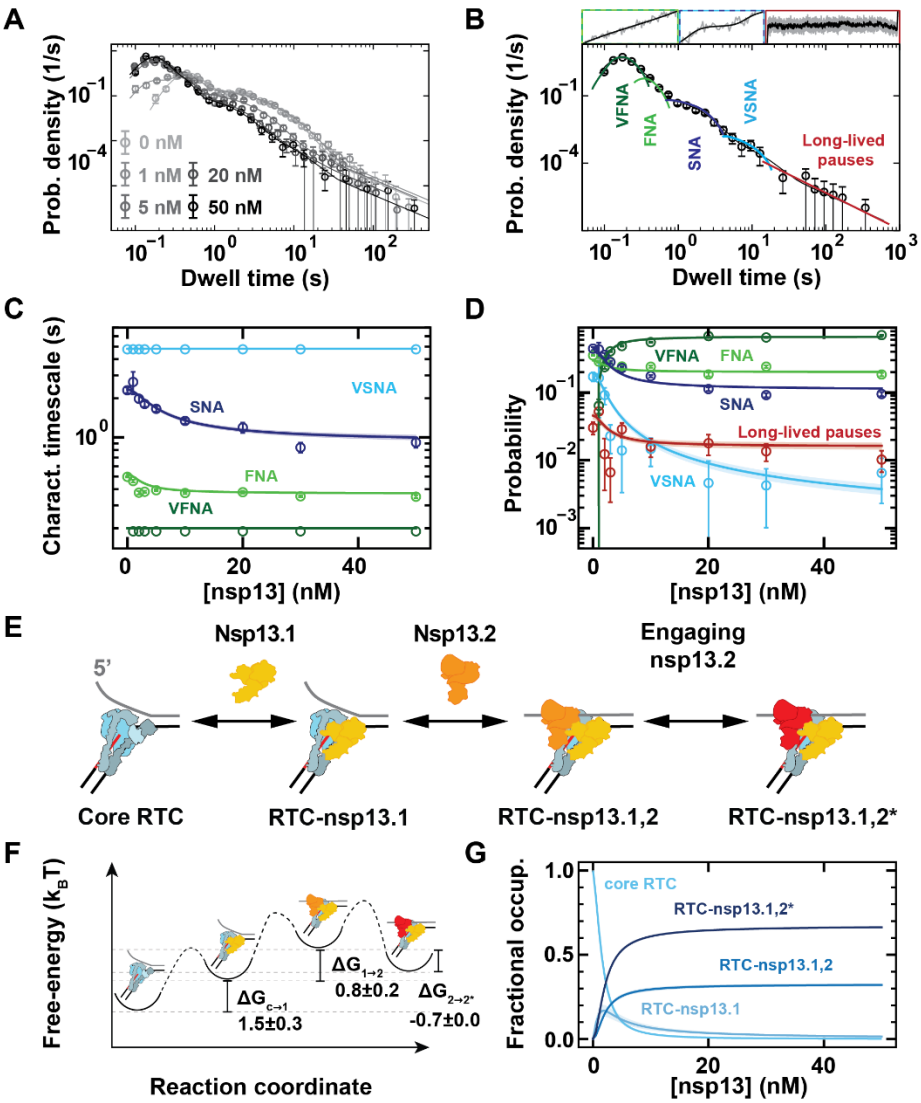

Figure 3: Assembly and stability of the SARS-CoV-2 RTC with nsp13-helicase. (A) Dwell-time distributions for RTC elongation at indicated nsp13-helicase concentrations with dwell-time fits (solid line, B) **(B)** The dwell-time fit-function consists of five probability density functions (pdf's): very fast, fast, slow and very slow nucleotide addition (VFNA, FNA, SNA, VSNA) and long-lived pauses. These pdf's are combined and fitted (black line) on the dwell-time distribution (circles) (**Materials and Methods**). The insets above are snapshots of characteristic traces for each timescale. The errorbars in (A, B) represent one standard deviation from 100 bootstraps of the dwell-times. **(C)** Characteristic timescales and **(D)** probabilities for the different pathways versus nsp13-helicase concentration for the different fits compared. The circles with errorbars and the solid lines with shaded areas represent the mean values and one standard deviation from 100 bootstraps of the dwell-time and RTC assembly model fits respectively. VFNA and VSNA characteristic timescales were fixed to 0.2 s and 4.8 s and therefore present no errorbars (**Materials and Methods**). **(E)** Schematic of the RTC assembly model. **(F)** The extracted free-energy landscape and **(G)** corresponding fractional occupancies versus nsp13-helicase concentration fitted on the dwell-time distributions with shaded areas as errorbars.

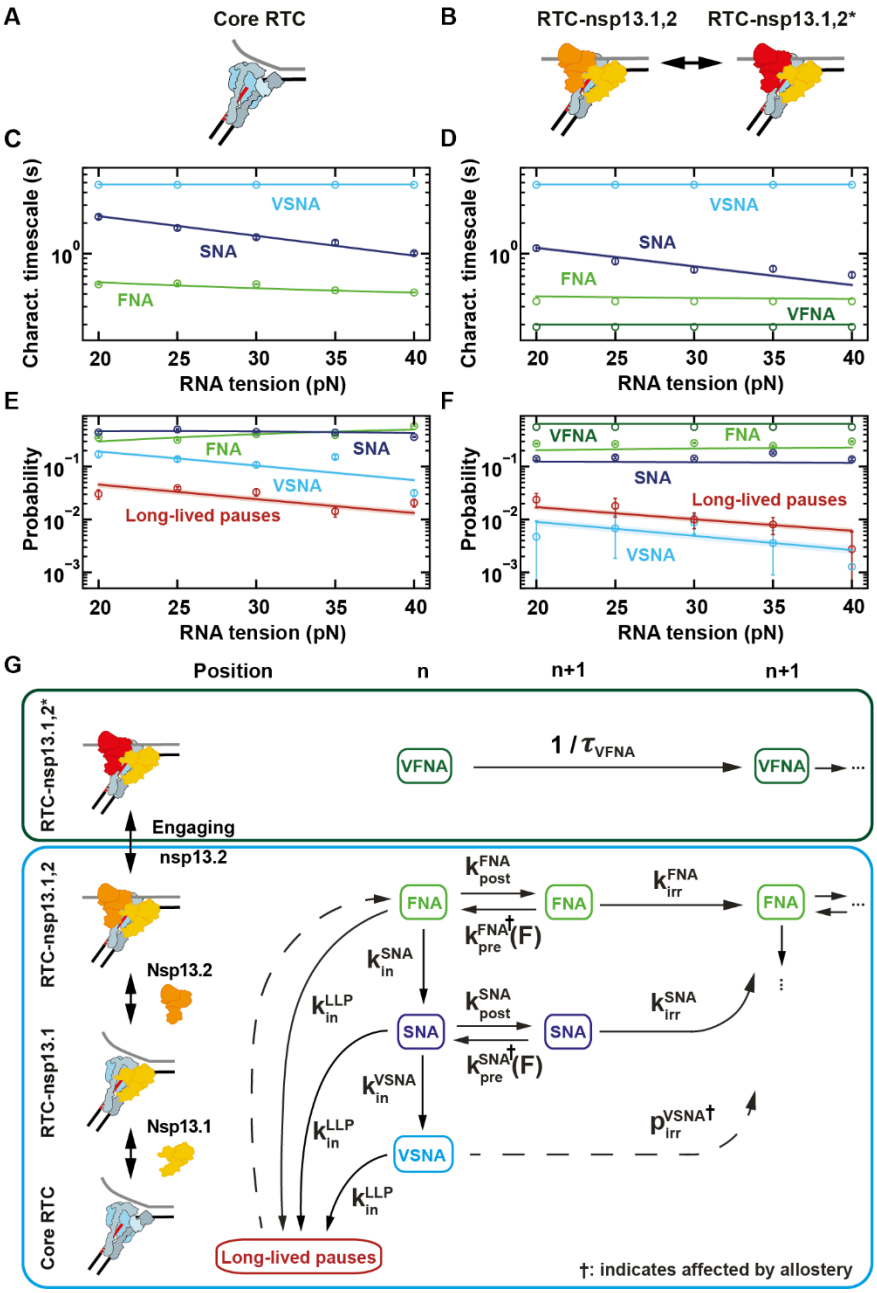

Figure 4: Mechanochemical model for the nucleotide addition cycle of the SARS-CoV-2 core RTC alone or in complex with nsp13-helicase. Schematic representation of the elongating RTC complexes **(A)** without and **(B)** with nsp13-helicase at saturating concentration. **(C, D)** Characteristic timescales and **(E, F)** Probabilities for the different nucleotide addition pathways (VFNA, FNA, SNA, VSNA) and long-lived pause versus the tension applied to the non-template RNA strand and either (C, E) without or (D, F) with saturating nsp13-helicase concentration. The circles with errorbars represent the mean value and one standard deviation from 100 bootstraps of the dwell-time fits. The solid lines and shaded areas represent the mean values and the region within one standard deviation of the mean obtained from 100 bootstraps of the global fit with the mechanochemical model shown in (G) (**Materials and Methods**). **(G)** Mechanochemical model underlying the timescales and probabilities (green box) for the VFNA pathway, which is only entered by RTC-nsp13.1,2* complex, and (blue box) for the nucleotide addition pathways entered by the core RTC, RTC-nsp13.1 and RTC-nsp13.1,2. Solid and dashed arrows respectively represent kinetic steps for which rates could either be extracted or not from the global fit.